

A Unified Framework for Dynamic Analysis of Tensegrity Structures with Arbitrary Rigid Bodies and Rigid Bars

Jiahui Luo^a, Zhigang Wu^a, Xiaoming Xu^{a,b,*}

^a School of Aeronautics and Astronautics, Sun Yat-sen University, No.66 Gongchang Road, Guangming District, Shenzhen, 518107, China

^b State Key Laboratory of Structural Analysis for Industrial Equipment, Dalian University of Technology, No.2 Linggong Road, Ganjingzi District, Dalian, 116024, China

Abstract

In this paper, we develop a unified framework to study the dynamics of tensegrity systems that can include any arbitrary rigid bodies and rigid bars. The natural coordinates are adopted as a completely non-minimal modeling approach to describe both rigid bodies and rigid bars in terms of different combinations of basic points and base vectors. Various types of coordinates combinations are then unified into polymorphic expressions which succinctly encompass Class-1-to- k tensegrities. Then, we employ the Lagrange-d'Alembert principle to derive the dynamic equation, which has a constant mass matrix and is free from trigonometric functions as well as centrifugal and Coriolis terms, owing to the non-minimal formulations. For numerical analysis of nonlinear dynamics, a modified symplectic integration scheme is derived, accommodating non-conservative forces and prescribed boundary conditions. Additionally, formulations for statics and linearized dynamics around static equilibrium states are derived to help determine cable actuations and calculate natural frequencies and mode shapes, which are commonly needed for structural analyses. Numerical examples are given to demonstrate the proposed approach's abilities in the modeling of tensegrity structures composed of Class-1-to- k modules and conducting dynamic simulations with complex conditions, including slack cables, gravity loads, seismic grounds, and cable-based deployments. Finally, two novel designs of tensegrity structures exemplify new ways to create multi-functional composite structures.

Keywords: tensegrity, dynamic modeling, natural coordinates, modal analysis, symplectic integration

1. Introduction

The term *tensegrity*, combining “tensile” and “integrity”, was coined by Buckminster Fuller [1] to describe a kind of prestressed structures, that were created by Ioganson and Snelson [2]. A commonly adopted definition is given by [3]: a tensegrity structure is a self-sustaining composition of rigid members and tensile members, and if there is at least a torqueless joint connecting k rigid members, it is called a Class- k tensegrity. Recent decades have witnessed two trends of developments in the tensegrity literature.

One trend is interested in a subset of tensegrity structures, where the rigid members are thin bars with negligible inertia about the longitudinal axis. Because this setting makes all members axial-loaded, i.e. in either tension or compression, material efficiency can be maximized. Consequently, these “bars-only” tensegrities are inherently strong and lightweight with the potential to minimal mass designs [3]. Mathematical elegance is also recognized, because both compressive and tensile members can be treated as the same elements, differing only in the signs of their force densities. Furthermore, many “bars-only” tensegrities are found to be deployable using simple cable-based actuators [4–6]. Thus, this trend of developments is mostly seen in civil engineering [7–9] and aerospace [10–12], etc. However, “bars-only” tensegrities are not without their problems: they usually have numerous bars and cables making them hard to fabricate and assemble; they have little capacity space in the interior; and the interfaces between tensegrity modules are complicated.

The other trend concerns tensegrities with rigid bodies, which are allowed to have complex shapes instead of being thin bars only. Tensegrities with rigid bodies can date back to the “X-Piece” (one of the earliest tensegrities created by Snelson [13]). Compared to the “bars-only” setting, they usually have fewer members and a larger interior space, while still being modular and compliant. Furthermore, they are recognized in biology to explain structural properties such as the interactions of muscles and bones [3, 7], and the integrity of vertebrate spines [14]. Thus, they are often used in the robotics literature to create bio-inspired designs, such as tensegrity joints [15] and tensegrity fishes [16], etc.

In recent years, an interest to merge these two trends is growing. For instance, Ref. [17] proposes a novel tensegrity robotic unit which combines a rigid triangular frame and a rigid bar to simplify topology. Ref. [18] devises topology-finding method to discover new structures like the tensegrity bridge, which have not only bars as supporting struts but also a rigid plate as the bridge deck. The motivation to integrate rigid bodies and rigid bars into one tensegrity structure

is the possibility to make their respective advantages complementary to each other. On the one hand, the rigid bars, when connected with cables, can provide high-strength and low-weight supporting as well as deployability. On the other hand, the rigid bodies in a tensegrity help to simplify the interfaces between different modules, to hold actuators and payloads, and to provide a certain degree of biomimetic functionalities.

Consequently, a unified framework for dynamic analyses of tensegrity structures including both arbitrary rigid bodies and rigid bars is called for. However, this “bodies-and-bars” setting presents difficulties due to the differences between them in 3D space. First, the vanishing inertia about the axis of a thin bar can lead to singular mass matrices [19]. Therefore, this thin-bar assumption is often relaxed to give some thickness to them, so that rigid body dynamics can be applied [20, 21]. Nonetheless, the rotation and angular velocity about the axis of a bar, either thin or thick, are still ill-defined. In other words, a 3D rigid bar has only five degrees of freedom (DoFs), one less than a 6-DoF 3D rigid body. Therefore, special treatments may be needed to determine the orientation parameters [22].

For “bars-only” tensegrities, a series of works [19, 23–27] develop specialized non-minimal formulations which use the nodal coordinates of two endpoints and a bar length constraint, i.e. six coordinates and one constraint, to uniquely define the dynamics of a 3D rigid bar, and thereby resolve these difficulties. Additionally, the non-minimal formulations are found to have other nice properties for dynamic analyses: the mass matrix is constant; velocity-dependent terms for centrifugal forces and Coriolis forces are vanished; and no trigonometric function is involved.

Therefore, in the “bodies-and-bars” setting of tensegrity structures, it would be beneficial to retain the non-minimal formulations of rigid bars. In line with this thought, a recent work [28] on the form-finding problems combines the nodal coordinates with minimal coordinates of rigid bodies to formulate static equilibrium equations. However, it has not developed dynamic equations, and the introduction of minimal coordinates can have “contaminating” effects on the formulations. For example, Euler angles are used as a minimal description of orientations [28], so trigonometric functions are unavoidable.

This paper develops a unified framework for dynamic analysis of tensegrity structures, where not only rigid bars but also arbitrary rigid bodies are described by non-minimal formulations through the natural coordinates [29–32]. In this way, the notable features of non-minimal formulations are preserved. Furthermore, the natural coordinates are comprehensively reformed better to suit the needs in the modeling of tensegrity structures. First, different types of coordinate combinations are exhaustively derived for arranging basic points and base vectors on 3D and 2D rigid bodies. This helps to reduce the number of coordinates and gives analysts more flexibility to model torqueless joints which are present in Class- k ($k>1$) tensegrity structures. Second, by use of polymorphism

*Corresponding author

Email addresses: luojiah3@mail2.sysu.edu.cn (Jiahui Luo), wuzhigang@mail.sysu.edu.cn (Zhigang Wu), xuxm29@mail1.sysu.edu.cn (Xiaoming Xu)

and conversions between the different types of coordinate combinations, the formulations of both rigid bodies and rigid bars in both 3D and 2D spaces are unified. This helps to write succinct mathematical expressions and is beneficial to implement generic computer codes. Third, a coordinate-separating strategy is devised to deal with fixed or moving boundary conditions.

Additionally, solution methods for static and dynamic analyses are derived. First, forward and inverse static analysis formulations are derived for the ease of complete analyses in the same framework. Second, linearized dynamics is derived to allow for modal analyses to calculate natural frequencies and mode shapes. Third, numerical analysis of nonlinear dynamics is enabled by a symplectic integration scheme, which is modified to accommodate non-conservative forces as well as prescribed coordinates.

Finally, two new tensegrity structures are studied to verify the proposed approach as well as to demonstrate the innovative possibilities of integrating rigid bodies and rigid bars into one tensegrity system.

The rest of this paper is organized as follows. Sec. 2 derives the unifying formulations for 3D and 2D rigid bodies and rigid bars, based on which Sec. 3 modeled the tensegrity structures. Secs. 4 and 5 derives solution methods for static and dynamic problems, respectively, followed by the numerical examples in Sec. 6. Finally, conclusions are drawn in Sec. 7.

2. Unifying rigid bodies and rigid bars using natural coordinates

In the following, rigid bodies and rigid bars are collectively called rigid members. They are indistinguishably labeled by circled numbers ①, ②, ..., or circled capital letters ①, ②, ..., etc. Thus, a capital subscript, such as (i) , denotes the label number of a rigid member.

2.1. Rigid bodies of arbitrary shapes

2.1.1. 3D rigid bodies

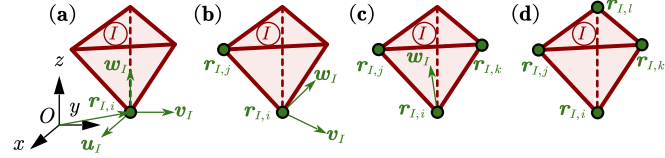


Figure 1: A 3D rigid body described by the (a) RUVW, (b) RRVW, (c) RRRW, and (d) RRRR type natural coordinates.

Consider a 3D rigid body in the shape of a tetrahedron, as shown in Fig. 1, where basic points $\mathbf{r}_{1,i}, \mathbf{r}_{1,j}, \mathbf{r}_{1,k}, \mathbf{r}_{1,l} \in \mathbb{R}^3$ and base vectors $\mathbf{u}_I, \mathbf{v}_I, \mathbf{w}_I \in \mathbb{R}^3$ are fixed on the rigid body and expressed in the global inertial frame. Four types of natural coordinates, i.e.

$$\begin{aligned} \mathbf{q}_{I,\text{ruvw}} &= [\mathbf{r}_{1,i}^T, \mathbf{u}_I^T, \mathbf{v}_I^T, \mathbf{w}_I^T]^T, & \mathbf{q}_{I,\text{rrvw}} &= [\mathbf{r}_{1,i}^T, \mathbf{r}_{1,j}^T, \mathbf{v}_I^T, \mathbf{w}_I^T]^T, \\ \mathbf{q}_{I,\text{rrrw}} &= [\mathbf{r}_{1,i}^T, \mathbf{r}_{1,j}^T, \mathbf{r}_{1,k}^T, \mathbf{w}_I^T]^T, & \text{and } \mathbf{q}_{I,\text{rrrr}} &= [\mathbf{r}_{1,i}^T, \mathbf{r}_{1,j}^T, \mathbf{r}_{1,k}^T, \mathbf{r}_{1,l}^T]^T, \end{aligned} \quad (1)$$

can be used to describe a 3D rigid body, corresponding to Fig. 1(a) to (d), respectively. while $(i)_{\text{ruvw}}$, etc, denote the type of natural coordinates. For the latter three types of natural coordinates, we can formally define $\mathbf{u}_I = \mathbf{r}_{1,j} - \mathbf{r}_{1,i}$, $\mathbf{v}_I = \mathbf{r}_{1,k} - \mathbf{r}_{1,i}$, and $\mathbf{w}_I = \mathbf{r}_{1,l} - \mathbf{r}_{1,i}$, so that they can be converted to the first type by

$$\mathbf{q}_{I,\text{ruvw}} = \mathbf{Y}_{\text{rrvw}} \mathbf{q}_{I,\text{rrvw}} = \mathbf{Y}_{\text{rrrw}} \mathbf{q}_{I,\text{rrrw}} = \mathbf{Y}_{\text{rrrr}} \mathbf{q}_{I,\text{rrrr}}, \quad (2)$$

where the conversion matrices are defined as, respectively,

$$\mathbf{Y}_{\text{rrvw}} = \begin{bmatrix} 1 & 0 & 0 & 0 \\ -1 & 1 & 0 & 0 \\ 0 & 0 & 1 & 0 \\ 0 & 0 & 0 & 1 \end{bmatrix} \otimes \mathbf{I}_3, \quad \mathbf{Y}_{\text{rrrw}} = \begin{bmatrix} 1 & 0 & 0 & 0 \\ -1 & 1 & 0 & 0 \\ -1 & 0 & 1 & 0 \\ 0 & 0 & 0 & 1 \end{bmatrix} \otimes \mathbf{I}_3, \quad \text{and } \mathbf{Y}_{\text{rrrr}} = \begin{bmatrix} 1 & 0 & 0 & 0 \\ -1 & 1 & 0 & 0 \\ -1 & 0 & 1 & 0 \\ -1 & 0 & 0 & 1 \end{bmatrix} \otimes \mathbf{I}_3 \quad (3)$$

Note that the base vectors are assumed to be non-coplanar, thus the natural coordinates actually form an affine frame attached to the 3D rigid body. Consequently, the position vector of a generic point on the 3D rigid body can be expressed by

$$\mathbf{r} = \mathbf{r}_{1,i} + c_{1,1}\mathbf{u}_I + c_{1,2}\mathbf{v}_I + c_{1,3}\mathbf{w}_I = \mathbf{C}_{I,\text{ruvw}} \mathbf{q}_{I,\text{ruvw}}, \quad (4)$$

where $\mathbf{C}_{I,\text{ruvw}} = [1, c_{1,1}, c_{1,2}, c_{1,3}] \otimes \mathbf{I}_3$ and $c_{1,1}, c_{1,2}$ and $c_{1,3}$ are the coordinates of the generic point in that affine frame.

To ensure rigidity of the body, the natural coordinates $\mathbf{q}_{I,\text{ruvw}}$ must satisfy six intrinsic constraints

$$\Phi_I(\mathbf{q}_{I,\text{ruvw}}) = \begin{pmatrix} \mathbf{u}_I^T \mathbf{u}_I - \bar{\mathbf{u}}_I^T \bar{\mathbf{u}}_I \\ \mathbf{v}_I^T \mathbf{v}_I - \bar{\mathbf{v}}_I^T \bar{\mathbf{v}}_I \\ \mathbf{w}_I^T \mathbf{w}_I - \bar{\mathbf{w}}_I^T \bar{\mathbf{w}}_I \\ \mathbf{v}_I^T \mathbf{w}_I - \bar{\mathbf{v}}_I^T \bar{\mathbf{w}}_I \\ \mathbf{u}_I^T \mathbf{w}_I - \bar{\mathbf{u}}_I^T \bar{\mathbf{w}}_I \\ \mathbf{u}_I^T \mathbf{v}_I - \bar{\mathbf{u}}_I^T \bar{\mathbf{v}}_I \end{pmatrix} \quad (5)$$

where $\bar{\mathbf{u}}_I, \bar{\mathbf{v}}_I$ and $\bar{\mathbf{w}}_I$ are the base vectors expressed in a body-fixed coordinate frame, and thus are constant.

2.1.2. 2D rigid bodies

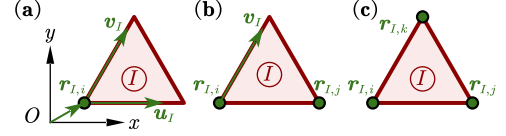


Figure 2: A 2D rigid body described by the (a) RUV, (b) RRV, and (c) RRR type natural coordinates.

Natural coordinates for a 2D rigid body are developed in the same vein as for the 3D case. Three types of natural coordinates, $\mathbf{q}_{I,\text{ruv}} = [\mathbf{r}_{1,i}^T, \mathbf{u}_I^T, \mathbf{v}_I^T]^T$, $\mathbf{q}_{I,\text{rrv}} = [\mathbf{r}_{1,i}^T, \mathbf{r}_{1,j}^T, \mathbf{v}_I^T]^T$, and $\mathbf{q}_{I,\text{rrr}} = [\mathbf{r}_{1,i}^T, \mathbf{r}_{1,j}^T, \mathbf{r}_{1,k}^T]^T$, corresponding to Fig. 2(a) to (c), respectively, are available for a 2D rigid body. The latter two types can be converted to the first type by

$$\mathbf{q}_{I,\text{ruv}} = \mathbf{Y}_{\text{rrv}} \mathbf{q}_{I,\text{rrv}} = \mathbf{Y}_{\text{rrr}} \mathbf{q}_{I,\text{rrr}} \quad (6)$$

with

$$\mathbf{Y}_{\text{rrv}} = \begin{bmatrix} 1 & 0 & 0 \\ -1 & 1 & 0 \\ 0 & 0 & 1 \end{bmatrix} \otimes \mathbf{I}_2 \quad \text{and} \quad \mathbf{Y}_{\text{rrr}} = \begin{bmatrix} 1 & 0 & 0 \\ -1 & 1 & 0 \\ -1 & 0 & 1 \end{bmatrix} \otimes \mathbf{I}_2. \quad (7)$$

The base vectors are assumed to be non-collinear. So the position vector of a generic point on the 2D rigid body can be expressed by

$$\mathbf{r} = \mathbf{r}_{1,i} + c_{1,1}\mathbf{u}_I + c_{1,2}\mathbf{v}_I = \mathbf{C}_{I,\text{ruv}} \mathbf{q}_{I,\text{ruv}} \quad (8)$$

where $\mathbf{C}_{I,\text{ruv}} = [1, c_{1,1}, c_{1,2}] \otimes \mathbf{I}_2$ and $c_{1,1}$ and $c_{1,2}$ are the coordinates of the generic point in the affine frame formed by the natural coordinates.

And the three intrinsic constraints that ensure the rigidity are

$$\Phi_I(\mathbf{q}_{I,\text{ruv}}) = \begin{pmatrix} \mathbf{u}_I^T \mathbf{u}_I - \bar{\mathbf{u}}_I^T \bar{\mathbf{u}}_I \\ \mathbf{v}_I^T \mathbf{v}_I - \bar{\mathbf{v}}_I^T \bar{\mathbf{v}}_I \\ \mathbf{u}_I^T \mathbf{v}_I - \bar{\mathbf{u}}_I^T \bar{\mathbf{v}}_I \end{pmatrix} \quad (9)$$

2.2. 3D and 2D rigid bars

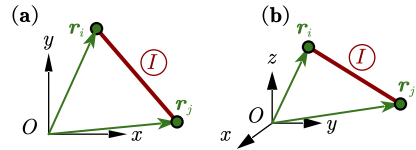


Figure 3: A (a) 2D or (b) 3D rigid bar described by the two endpoints. Rigid bars are drawn as thick black lines. Endpoints are colored in green.

A rigid bar can be described by its two endpoints, in either 2D or 3D space, as shown in Fig. 3(a) and (b), respectively. The position vectors of the endpoints in the global inertial frame are denoted by $\mathbf{r}_{1,i}$ and $\mathbf{r}_{1,j} \in \mathbb{R}^m$, respectively. Then, the natural coordinates of the rigid bar is the concatenation $\mathbf{q}_{I,\text{rr}} = [\mathbf{r}_{1,i}^T, \mathbf{r}_{1,j}^T]^T \in \mathbb{R}^{2m}$. In order to have similar formulations as in Sec. 2.1, we convert $\mathbf{q}_{I,\text{rr}}$ to the standard type $\mathbf{q}_{I,\text{ru}} = [\mathbf{r}_I^T, \mathbf{u}_I^T]^T \in \mathbb{R}^{2m}$ by

$$\mathbf{q}_{I,\text{ru}} = \mathbf{Y}_{\text{rr}} \mathbf{q}_{I,\text{rr}} \quad \text{with} \quad \mathbf{Y}_{\text{rr}} = \begin{bmatrix} -1 & 0 \\ -1 & 1 \end{bmatrix} \otimes \mathbf{I}_m \quad (10)$$

The position vector of a generic point along the axis of the rigid bar is given by

$$\mathbf{r} = \mathbf{r}_{1,i} + c_I \mathbf{u} = \mathbf{C}_{I,\text{ru}} \mathbf{q}_{I,\text{ru}} \quad (11)$$

where $C_{l,ru} = [1, c_l] \otimes \mathbf{I}_m$ and the coefficient c depends on the relative position of the generic point to the point i .

Because the length of the rigid bar, denoted by b_l , should remain unchanged, an intrinsic constraint is imposed as

$$\Phi_l(\mathbf{q}_{l,ru}) = \mathbf{u}_l^T \mathbf{u}_l - b_l \quad \text{and} \quad A_l(\mathbf{q}_{l,ru}) = \frac{\partial \Phi_l}{\partial \mathbf{q}_{l,ru}} = [\mathbf{0}^T, 2\mathbf{u}_l^T] \quad (12)$$

2.3. Unified formulations and mass matrices

The relations (4), (8), and (11) can be put in a unifying form

$$\mathbf{r} = \mathbf{C}_l \mathbf{q}_l, \quad (13)$$

with a polymorphic transformation matrix

$$\mathbf{C}_l = [1, \mathbf{c}_l^T] \otimes \mathbf{I}_m \quad (14)$$

which plays a central role in the following derivations. Hereafter, we will drop the subscripts (tr) , (ruv) , and (ruvw) , etc. to indicate that the formulations are valid for any rigid members, and, by conversions (2) and (6), for any types of natural coordinates. But one must keep in mind that the specific expressions, e.g. C_l , correspond to the type of \mathbf{q}_l .

The linear relations (2), (6), and (10) allow straightforward conversions from the formulations for one type of natural coordinates to those for another. Therefore, the following derivations will be centered around the standard types RUVW, RUV, and RU.

For the rigid member \textcircled{I} , let ρ_l denotes its density, which can be either linear, area, or volume density corresponding to the rigid member's type. Then, the kinetic energy can be computed by an integral over its entire domain Ω as

$$T_l = \frac{1}{2} \int_{\Omega} \rho_l \dot{\mathbf{r}}^T \dot{\mathbf{r}} d\Omega = \frac{1}{2} \int_{\Omega} \rho_l \dot{\mathbf{q}}_l^T \mathbf{C}_l^T \mathbf{C}_l \dot{\mathbf{q}}_l d\Omega = \frac{1}{2} \dot{\mathbf{q}}_l^T \mathbf{M}_l \dot{\mathbf{q}}_l \quad (15)$$

where (13) are used for the second equality, and

$$\begin{aligned} \mathbf{M}_l &= \int_{\Omega} \rho_l \mathbf{C}_l^T \mathbf{C}_l d\Omega = \int_{\Omega} \left(\rho_l \begin{bmatrix} 1 & \mathbf{c}_l^T \\ \mathbf{c}_l & \mathbf{c}_l \mathbf{c}_l^T \end{bmatrix} \right) d\Omega \otimes \mathbf{I}_m \\ &= \begin{bmatrix} \int_{\Omega} \rho_l d\Omega & \int_{\Omega} \rho_l \mathbf{c}_l^T d\Omega \\ \int_{\Omega} \rho_l \mathbf{c}_l d\Omega & \int_{\Omega} \rho_l \mathbf{c}_l \mathbf{c}_l^T d\Omega \end{bmatrix} \otimes \mathbf{I}_m \end{aligned} \quad (16)$$

is a constant mass matrix.

3. Modeling tensegrity systems

3.1. Pin joints and ball joints

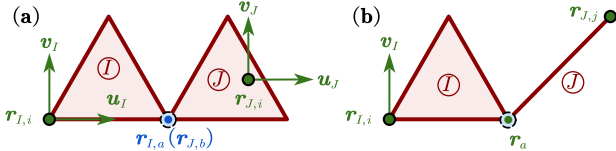


Figure 4: Two 2D rigid bodies connected by a pin joint, which is represented by a dash-line circle. The point coinciding with the joint axis is colored in blue.

A Class- k ($k > 1$) tensegrity system allows the use of pin joints (or ball joints in the 3D case), each of which can connect up to k different rigid members. Depending on the placements of basic points, there are two modeling methods.

The first is a general method, as exemplified by Fig. 4(a), where a frictionless pin joint pins point a of rigid body \textcircled{I} on point b of rigid body \textcircled{J} , and consequently imposing a set of extrinsic constraints

$$\Phi^{\text{ex}}(\mathbf{q}_l, \mathbf{q}_j) = \mathbf{r}_{l,a} - \mathbf{r}_{j,b} = \mathbf{C}_{l,a} \mathbf{q}_l - \mathbf{C}_{j,b} \mathbf{q}_j = \mathbf{0}, \quad (17)$$

where (13) is used for the second equality, and the natural coordinates of the two rigid bodies are $\mathbf{q}_l = [\mathbf{r}_{l,i}^T, \mathbf{u}_l^T, \mathbf{v}_l^T]^T$ and $\mathbf{q}_j = [\mathbf{r}_{j,i}^T, \mathbf{u}_j^T, \mathbf{v}_j^T]^T$, respectively.

The second method is to share the basic points between rigid members, as exemplified by Fig. 4(b), where a pin joint is located at the basic point a . So we have natural coordinates $\mathbf{q}_l = [\mathbf{r}_{l,i}^T, \mathbf{r}_a^T, \mathbf{v}_l^T]^T$ for the 2D rigid body \textcircled{I} , and $\mathbf{q}_j = [\mathbf{r}_a^T, \mathbf{r}_{j,j}^T]^T$ for the 2D rigid bar \textcircled{J} : they share the vector \mathbf{r}_a . This method has computational advantages over the first one, because it needs no extrinsic

constraints and it reduces the number of system's coordinates. However, it requires extra effort to judiciously choose the types of natural coordinates and the placements of basic points. And, due to the limited number of basic points (two, three, or four for a rigid bar, a 2D, or 3D rigid body, respectively), a combination of the two methods would still be needed in some cases.

If a pin joint connects k ($k > 2$) rigid members, it can be modeled as $k-1$ pin joints overlapping at one place.

Ball joints in the 3D case can be modeled in the same way, owing to the unifying form (13).

3.2. Prescribed rigid members and points

In practice, most tensegrity systems have some members with prescribed motions, such that their positions, velocities, and accelerations are either partly or entirely given. For example, a rigid member could be pin-jointed to a base, or a cable could have its one endpoint tied to the ground. It would be cumbersome to derive case-by-case formulations for these prescribed rigid members and endpoints. Alternatively, we can extend the above derivations, but also without loss of flexibility, by separating the prescribed and free (unprescribed) coordinates. To do this, let's denote the numbers of prescribed, free, and total coordinates for the rigid member \textcircled{I} by \tilde{n}_l , \hat{n}_l , and $n_l = \tilde{n}_l + \hat{n}_l$, respectively, and for the system by \tilde{n} , \hat{n} , and $n = \tilde{n} + \hat{n}$, respectively. Then, the separation and reintegration of the coordinates of the rigid member \textcircled{I} and of the system are defined by

$$\begin{pmatrix} \tilde{\mathbf{q}}_l \\ \hat{\mathbf{q}}_l \end{pmatrix} = \begin{bmatrix} \tilde{\mathbf{E}}_l^T \\ \hat{\mathbf{E}}_l^T \end{bmatrix} \mathbf{q}_l, \quad \mathbf{q}_l = \begin{bmatrix} \tilde{\mathbf{E}}_l \\ \hat{\mathbf{E}}_l \end{bmatrix} \begin{pmatrix} \tilde{\mathbf{q}}_l \\ \hat{\mathbf{q}}_l \end{pmatrix}, \quad \begin{pmatrix} \tilde{\mathbf{q}} \\ \hat{\mathbf{q}} \end{pmatrix} = \begin{bmatrix} \tilde{\mathbf{E}}^T \\ \hat{\mathbf{E}}^T \end{bmatrix} \mathbf{q}, \quad \text{and} \quad \mathbf{q} = \begin{bmatrix} \tilde{\mathbf{E}} \\ \hat{\mathbf{E}} \end{bmatrix} \begin{pmatrix} \tilde{\mathbf{q}} \\ \hat{\mathbf{q}} \end{pmatrix}, \quad (18)$$

where $\tilde{\mathbf{q}}_l \in \mathbb{R}^{\tilde{n}_l}$ and $\hat{\mathbf{q}}_l \in \mathbb{R}^{\hat{n}_l}$ are prescribed coordinates; $\tilde{\mathbf{q}} \in \mathbb{R}^{\tilde{n}}$ and $\hat{\mathbf{q}} \in \mathbb{R}^{\hat{n}}$ are free coordinates; $[\tilde{\mathbf{E}}_l, \hat{\mathbf{E}}_l] \in \mathbb{Z}^{n_l \times n_l}$ and $[\tilde{\mathbf{E}}, \hat{\mathbf{E}}] \in \mathbb{Z}^{n \times n}$, are constant orthonormal matrices that only have zeros and ones as elements.

Additionally, let's define a special coordinates vector $\mathbf{q}_0^T = [\tilde{r}_{0,1}^T, \dots, \tilde{r}_{0,\tilde{n}_p}^T]^T$ containing a list of \tilde{n}_p prescribed points. And, for the sake of consistency, define $\tilde{n}_0 = 0$, $n_0 = \tilde{n}_0 = m \times \tilde{n}_p$, and $\mathbf{C}_{0,i} = \mathbf{c}_0^T \otimes \mathbf{I}_m$, where $\mathbf{c}_0 \in \mathbb{Z}^{\tilde{n}_p}$ are zeros except that the i th element equals to 1. Consequently, $\tilde{\mathbf{E}}_0$ is an identity matrix and $\hat{\mathbf{E}}_0$ is an empty matrix, and the \textcircled{I} prescribed point can be expressed in the same form of (13) as

$$\mathbf{r}_{0,i} = \tilde{\mathbf{r}}_{0,i} = \mathbf{C}_{0,i} \mathbf{q}_0, \quad \text{for } i = 1, \dots, \tilde{n}_p. \quad (19)$$

The relations between the system's coordinates and those of rigid members and prescribed points are given by

$$\mathbf{q}_l = \mathbf{T}_l \mathbf{q} = \tilde{\mathbf{T}}_l \tilde{\mathbf{q}} + \hat{\mathbf{T}}_l \hat{\mathbf{q}}, \quad \text{for } l = 0, \dots, n_b, \quad (20)$$

where \mathbf{T}_l , $\tilde{\mathbf{T}}_l = \mathbf{T}_l \tilde{\mathbf{E}}$, and $\hat{\mathbf{T}}_l = \mathbf{T}_l \hat{\mathbf{E}}$ are constant matrices that select the right elements from the system, and also properly embody the sharing of basic points as presented in Sec. 3.1. Consequently, the relations for velocities and accelerations are simply $\dot{\mathbf{q}}_l = \mathbf{T}_l \dot{\mathbf{q}}$ and $\ddot{\mathbf{q}}_l = \mathbf{T}_l \ddot{\mathbf{q}}$, respectively. On the other hand, the variation should exclude the prescribed coordinates as

$$\delta \mathbf{q}_l = \hat{\mathbf{T}}_l \delta \hat{\mathbf{q}}. \quad (21)$$

Note that the relations (18) and (20) are actually implemented as index-selecting methods in the computer code, so that expensive matrix multiplications are avoided.

Last but not the least, any intrinsic constraints in (5), (9), and (12) and extrinsic constraints in (17) that contain no free coordinates should be dropped. The remaining constraints are collected by $\Phi(\mathbf{q})$, whose Jacobian matrix is defined by $\dot{\mathbf{A}}(\mathbf{q}) = \partial \Phi / \partial \dot{\mathbf{q}}$.

3.3. Generalized forces

Using (13) and (19) to (21), the position and its variation of a point of action p on the rigid member \textcircled{I} are, respectively,

$$\mathbf{r}_{l,p} = \mathbf{C}_{l,p} \mathbf{T}_l \mathbf{q} \quad \text{and} \quad \delta \mathbf{r}_{l,p} = \mathbf{C}_{l,p} \hat{\mathbf{T}}_l \delta \hat{\mathbf{q}}. \quad (22)$$

Consider a concentrated force $\mathbf{f}_{l,p}$ exerted on point p , as shown on the left of Fig. 5, the virtual work $\delta W_{l,p}$ done by $\mathbf{f}_{l,p}$ is $\delta W_{l,p} = \delta \mathbf{r}_{l,p}^T \mathbf{f}_{l,p} = \delta \hat{\mathbf{q}}^T \tilde{\mathbf{F}}_{l,p}$, where

$$\tilde{\mathbf{F}}_{l,p} = \hat{\mathbf{T}}_l^T \mathbf{C}_{l,p}^T \mathbf{f}_{l,p} \quad (23)$$

is the generalized force for $\mathbf{f}_{l,p}$.

In particular, the gravity force $\mathbf{f}_{l,g}$ is exerted on the mass center $\mathbf{r}_{l,g}$. Therefore, the generalized gravity force for the rigid member \textcircled{I} is given by $\tilde{\mathbf{F}}_{l,g} = \hat{\mathbf{T}}_l^T \mathbf{C}_{l,g}^T \mathbf{f}_{l,g}$, which is a constant vector.

Also note that (23) still holds for a prescribed point, because in that case $\tilde{\mathbf{T}}_l$ would be a zero matrix.

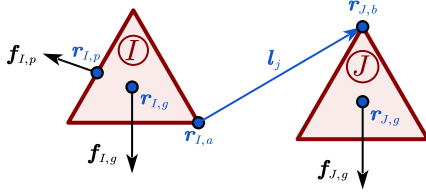


Figure 5: Two 2D rigid bodies subjected to gravity, a concentrated force, and tension forces of a cable. The points of action are colored in blue.

3.4. Tensile cables

Suppose the j th cable connects point a of the rigid member \textcircled{I} and point b of the rigid member \textcircled{J} , as shown in Fig. 5. It can be represented by a vector

$$\mathbf{l}_j = \mathbf{r}_{J,b} - \mathbf{r}_{I,a} = \mathbf{C}_{J,b} \mathbf{T}_J \mathbf{q} - \mathbf{C}_{I,a} \mathbf{T}_I \mathbf{q} = \mathbf{J}_j \mathbf{q} \quad (24)$$

where we use (22) and $\mathbf{J}_j = \mathbf{C}_{J,b} \mathbf{T}_J - \mathbf{C}_{I,a} \mathbf{T}_I$ is a constant matrix. Consequently, the current length and its time derivative of the cable are given by, respectively,

$$l_j = \sqrt{\mathbf{l}_j^T \mathbf{l}_j} = \sqrt{\mathbf{q}^T \mathbf{U}_j \mathbf{q}} \quad \text{and} \quad \dot{l}_j = \frac{\mathbf{l}_j^T \dot{\mathbf{l}}_j}{\sqrt{\mathbf{l}_j^T \mathbf{l}_j}} = \frac{(\mathbf{q}^T \mathbf{U}_j \dot{\mathbf{q}})}{l_j}, \quad (25)$$

where $\mathbf{U}_j = \mathbf{J}_j^T \mathbf{J}_j$ is also constant.

Define the force density by $\gamma_j = f_j/l_j$, where f_j is the tension force magnitude. So the tension force is given by either $\mathbf{f}_j = f_j \hat{\mathbf{l}}_j$ or $\mathbf{f}_j = \gamma_j \mathbf{l}_j$, where $\hat{\mathbf{l}}_j = \mathbf{l}_j/l_j$ is the unit direction vector.

Note that a cable generates a pair of tension forces exerted on point a and b with opposite directions. Therefore, according to (23), the generalized tension force for the j th cable reads

$$\dot{\mathbf{Q}}_j = \check{\mathbf{T}}_I^T \mathbf{C}_{I,a}^T \mathbf{f}_j - \check{\mathbf{T}}_J^T \mathbf{C}_{J,b}^T \mathbf{f}_j = -\check{\mathbf{E}}^T \mathbf{J}_j^T \mathbf{f}_j \quad (26)$$

Consequently, the system's tension force is the sum over all cables

$$\dot{\mathbf{Q}} = \sum_{j=1}^{n_c} (-\check{\mathbf{E}}^T \mathbf{J}_j^T \mathbf{f}_j) = -\check{\mathbf{E}}^T \bigoplus_{j=1}^{n_c} (\mathbf{J}_j^T \mathbf{l}_j) \boldsymbol{\gamma} \quad (27)$$

where $\boldsymbol{\gamma} = [\gamma_1, \dots, \gamma_{n_c}]^T$ collects the force densities and \oplus means the direct sum of matrices. Expression (27) shows the system's generalized tension force is linear in the cables' force densities. This notable property is also found in the dynamics framework for "bars-only" tensegrities by Skelton et al. [19, 25]. It is beneficial for the design of control schemes, which, however, will not be elaborated in this paper and subject to further research.

Expression (27) allows any constitutive laws of the cables. In the following, we adopt a common practice by assuming linear stiffness, linear damping, and a slacking behavior. Denote the rest length by μ_j , the stiffness coefficient by κ_j , the damping coefficient by η_j . Then, the tension force magnitude is given by

$$f_j = \begin{cases} f_j^+, & \text{if } f_j^+ \geq 0 \text{ and } l_j \geq \mu_j \\ 0, & \text{else} \end{cases} \quad \text{with } f_j^+ = \kappa_j(l_j - \mu_j) + \eta_j \dot{l}_j. \quad (28)$$

4. Static analysis formulations

Suppose a potential $V(\mathbf{q})$ is given as a function of the system's total coordinates, then the generalized potential force is given by $\check{\mathbf{G}} = -\partial V(\mathbf{q})/\partial \check{\mathbf{q}}^T$. Because $\check{\boldsymbol{\Phi}}$ is holonomic, we can define the augmented potential function as $\Pi = V - \boldsymbol{\Phi}^T \boldsymbol{\lambda}$, where $\boldsymbol{\lambda}$ is the Lagrange multipliers. Then, according to Lagrange-d'Alembert principle, we have the static equation of the system:

$$\begin{cases} -\check{\mathbf{Q}} - \check{\mathbf{F}}^{\text{ex}} + \frac{\partial \Pi}{\partial \check{\mathbf{q}}^T} = -\check{\mathbf{F}} - \check{\mathbf{A}}^T \boldsymbol{\lambda} = \mathbf{0} & (29a) \\ -\frac{\partial \Pi}{\partial \boldsymbol{\lambda}^T} = \check{\boldsymbol{\Phi}} = \mathbf{0} & (29b) \end{cases}$$

where $\check{\mathbf{F}} = \check{\mathbf{G}} + \dot{\mathbf{Q}} + \check{\mathbf{F}}^{\text{ex}}$ includes the generalized potential force $\check{\mathbf{G}}$, the generalized tension force $\dot{\mathbf{Q}}$, and any other external generalized forces $\check{\mathbf{F}}^{\text{ex}}$.

We should point out that, as long as the constitutive law of the cables can be transformed into polynomials, the static equation (29) is compatible with our previous work [33] on the *forward* statics problems of tensegrity systems, which are readily solved by the homotopy continuation method, and therefore will not be elaborated here.

For *inverse* statics problems, which solve for the cable variables from a known configuration of the system, it is convenient to eliminate the constraint forces first. To do this, define a matrix $\check{\mathbf{N}}$ whose columns are a set of linearly independent basis vectors of the nullspace of $\check{\mathbf{A}}$, such that $\check{\mathbf{A}} \check{\mathbf{N}} = \mathbf{0}$. Then, left-multiplying (29a) by $\check{\mathbf{N}}^T$ and using (27) lead to

$$\check{\mathbf{N}}^T \check{\mathbf{E}}^T \bigoplus_{j=1}^{n_c} (\mathbf{J}_j^T \mathbf{l}_j) \boldsymbol{\gamma} = \check{\mathbf{N}}^T (\check{\mathbf{G}} + \check{\mathbf{F}}^{\text{ex}}), \quad (30)$$

which are a set of linear equations for the force densities $\boldsymbol{\gamma}$. After solving (30), the Lagrange multipliers can be recovered from $\boldsymbol{\lambda} = (\check{\mathbf{A}} \check{\mathbf{N}}^T)^{-1} \check{\mathbf{A}} \check{\mathbf{F}}$.

When the constitutive law (28) is adopted and the inverse statics (30) is employed to solve for the rest lengths of cables, the following formulations can be used. Let $\boldsymbol{\ell} = [l_1, \dots, l_{n_c}]^T$ and $\boldsymbol{\mu} = [\mu_1, \dots, \mu_{n_c}]^T$ collect the lengths and rest lengths, respectively, of all cables. Suppose the cables are in tension, then the force density is given by

$$\gamma_j = f_j/l_j = k_j(l_j - \mu_j)/l_j \quad (31)$$

Substituting (31) into (30) and rearranging the terms, we have a system of linear equations about the rest lengths $\boldsymbol{\mu}$:

$$\mathbf{B} \boldsymbol{\mu} = \mathbf{b} \quad (32)$$

where matrix \mathbf{B} and vector \mathbf{b} are given by, respectively,

$$\mathbf{B} = \check{\mathbf{N}}^T \check{\mathbf{E}}^T \bigoplus_{j=1}^{n_c} (\mathbf{J}_j^T k_j \hat{\mathbf{l}}_j) \quad \text{and} \quad \mathbf{b} = \check{\mathbf{N}}^T \check{\mathbf{E}}^T \bigoplus_{j=1}^{n_c} (\mathbf{J}_j^T k_j \hat{\mathbf{l}}_j) \boldsymbol{\ell} - \check{\mathbf{N}}^T (\check{\mathbf{G}} + \check{\mathbf{F}}^{\text{ex}}) \quad (33)$$

5. Dynamic analysis formulations

5.1. Dynamic equation

The system's kinetic energy is simply the sum over all rigid member $T = \sum_{I=1}^{n_b} T_I = \frac{1}{2} \check{\mathbf{q}}^T \mathbf{M} \check{\mathbf{q}}$, where $\mathbf{M} = \sum_{I=1}^{n_b} \mathbf{T}_I^T \mathbf{M}_I \mathbf{T}_I$. However, the generalized inertia force must be derived with respect to the free coordinates as

$$\frac{d}{dt} \left(\frac{\partial T}{\partial \check{\mathbf{q}}^T} \right) = \frac{d}{dt} (\check{\mathbf{M}} \check{\mathbf{q}}) = \frac{d}{dt} (\check{\mathbf{M}} (\check{\mathbf{E}} \dot{\mathbf{q}} + \check{\mathbf{E}} \ddot{\mathbf{q}})) = \check{\mathbf{M}} \ddot{\mathbf{q}} + \check{\mathbf{M}} \dot{\check{\mathbf{q}}} \quad (34)$$

where $\check{\mathbf{M}} = \check{\mathbf{E}}^T \mathbf{M}$, $\check{\mathbf{M}} = \check{\mathbf{M}} \check{\mathbf{E}}$, and $\check{\mathbf{M}} = \check{\mathbf{M}} \check{\mathbf{E}}$ are different mass matrices that will be used later. For the dynamics of a tensegrity system, the Lagrange-d'Alembert principle states that the virtual work vanishes for all inertial forces, generalized forces, and constraint forces acting on the virtual displacement:

$$\delta \check{\mathbf{q}}^T (\check{\mathbf{M}} \ddot{\mathbf{q}} + \check{\mathbf{M}} \dot{\check{\mathbf{q}}}) - \delta \check{\mathbf{q}}^T \check{\mathbf{F}} - \delta \check{\mathbf{q}}^T \check{\mathbf{A}}^T \boldsymbol{\lambda} = 0 \quad (35)$$

Noting that $\forall \delta \check{\mathbf{q}} \in \check{\mathbf{N}}$, (35) leads to the Lagrange's equation of the first kind

$$\begin{cases} \check{\mathbf{M}} \ddot{\mathbf{q}} + \check{\mathbf{M}} \dot{\check{\mathbf{q}}} - \check{\mathbf{G}}(\mathbf{q}) - \dot{\mathbf{Q}}(\mathbf{q}, \dot{\mathbf{q}}, \boldsymbol{\mu}) - \check{\mathbf{F}}^{\text{ex}}(\mathbf{q}, \dot{\mathbf{q}}, t) - \check{\mathbf{A}}^T(\mathbf{q}) \boldsymbol{\lambda} = \mathbf{0} & (36a) \\ \check{\boldsymbol{\Phi}}(\mathbf{q}) = \mathbf{0} & (36b) \end{cases}$$

where the dependency is explicated, and the rest lengths $\boldsymbol{\mu}$ will be used as actuation values. One should also keep in mind that \mathbf{q} and $\dot{\mathbf{q}}$ contain prescribed coordinates $\check{\mathbf{q}}$ and $\dot{\check{\mathbf{q}}}$, which, along with $\ddot{\check{\mathbf{q}}}$, are interpreted as known functions of time t .

Thanks to the use of natural coordinates, the dynamic equation (36) gets rid of trigonometric functions as well as centrifugal and Coriolis terms, leaving a constant mass matrix.

For later use, the differential part (36a) can be rewritten as

$$\dot{\check{\mathbf{p}}} - \check{\mathbf{F}} - \check{\mathbf{A}}^T \boldsymbol{\lambda} = \mathbf{0} \quad (37)$$

where $\check{\mathbf{p}} = \partial T / \partial \dot{\check{\mathbf{q}}}^T = \check{\mathbf{M}} \dot{\check{\mathbf{q}}}$ is the generalized momentum.

5.2. Linearized dynamics around static equilibrium

Consider a system's state with small perturbations in the free coordinates and Lagrange multipliers as

$$\mathbf{q} = \mathbf{q}_e + \check{\mathbf{E}} \delta \check{\mathbf{q}}, \quad \dot{\mathbf{q}} = \dot{\mathbf{q}}_e + \check{\mathbf{E}} \delta \dot{\check{\mathbf{q}}}, \quad \ddot{\mathbf{q}} = \ddot{\mathbf{q}}_e + \check{\mathbf{E}} \delta \ddot{\check{\mathbf{q}}}, \quad \text{and} \quad \boldsymbol{\lambda} = \boldsymbol{\lambda}_e + \delta \boldsymbol{\lambda}, \quad (38)$$

where $\dot{q}_e = \ddot{q}_e = \mathbf{0}$, and (q_e, λ_e) satisfies the static equation (29). Substituting (38) into (36) and expanding it in Taylor series to the first order lead to

$$\begin{cases} \check{M}\delta\ddot{q} - \frac{\partial\check{F}}{\partial\dot{q}}\delta\dot{q} - \frac{\partial\check{F}}{\partial q}\delta q - \frac{\partial(\check{A}^T\lambda_e)}{\partial\dot{q}}\delta\dot{q} - \check{A}^T\delta\lambda = \mathbf{0} \\ \check{A}\delta\dot{q} = \mathbf{0} \end{cases} \quad (39a)$$

Recall that \check{N} is a basis of the nullspace of \check{A} . So left-multiplying (39a) by \check{N}^T eliminates the last term. And (39b) is solved by $\delta\dot{q} = \check{N}\xi$, where ξ are independent variables, which is then substituted back to (39a) to yield

$$\mathcal{M}\xi + C\xi + \mathcal{K}\xi = \mathbf{0} \quad (40)$$

where

$$\mathcal{M} = \check{N}^T\check{M}\check{N}, \quad C = \check{N}^T\left(\frac{-\partial\check{F}}{\partial\dot{q}}\right)\check{N}, \quad \text{and} \quad \mathcal{K} = \check{N}^T\left(\frac{-\partial\check{F}}{\partial q} - \frac{\partial(\check{A}^T\lambda_e)}{\partial\dot{q}}\right)\check{N} \quad (41)$$

are the reduced-basis mass matrix, reduced-basis tangent damping matrix, and reduced-basis tangent stiffness matrix, respectively.

At this point, we have a standard linear dynamic system (40), which can be used for the modal analysis of general tensegrity structures. For simplicity, consider free vibration with no damping ($C = \mathbf{0}$) and no external forces ($F^{\text{ex}} = \mathbf{0}$), then the solution to (40) boils down to the generalized eigenvalue problem

$$(\mathcal{K} - \omega_{(r)}^2\mathcal{M})\xi_{(r)} = \mathbf{0} \quad (42)$$

where $\omega_{(r)}$ is the natural frequency of the r th mode; $\xi_{(r)}$ is the mode shapes in the independent variables, which can be normalized with respect to mass by $\hat{\xi}_{(r)} = \frac{1}{\sqrt{m_{(r)}}}\xi_{(r)}$, where $m_{(r)} = \xi_{(r)}^T\mathcal{M}\xi_{(r)}$. Then, the mode shapes in the natural coordinates can be obtained through

$$q_{(r)} = q_e + \check{E}\delta\hat{\xi}_{(r)} = q_e + \check{E}\check{N}\hat{\xi}_{(r)} \quad (43)$$

5.3. Numerical analysis of nonlinear dynamics

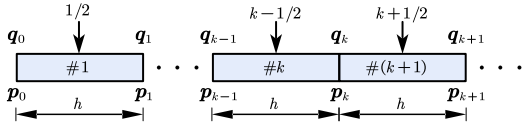


Figure 6: Equally spaced segments of the time domain. Each segment has two endpoints and one midpoint. The state vector (q_k, p_k) is located at endpoint k .

For numerical analysis of nonlinear dynamics, a symplectic integration scheme [34, 35] for differential-algebraic equations (DAEs) is revised to accommodate non-conservative forces and prescribed coordinates.

As illustrated in Fig. 6, the time domain is divided into equally spaced segments, where h is the timestep and (q_k, p_k) denotes the state vector at the segments' endpoints. At each endpoint, we demand that the differential equation (37) holds as

$$\dot{p}_k - \check{F}_k - \check{A}^T(q_k)\lambda_k = \mathbf{0} \quad (44)$$

Then, using central difference approximations

$$\begin{aligned} \dot{p}_k &\approx \frac{1}{h}(\check{p}_{k+1/2} - \check{p}_k + \check{p}_k - \check{p}_{k-1/2}), \quad \check{F}_k \approx \frac{1}{2}(\check{F}_{k-1/2} + \check{F}_{k+1/2}), \quad \text{and} \\ \lambda_k &\approx \frac{1}{2}(\lambda_{k-1/2} + \lambda_{k+1/2}) \end{aligned} \quad (45)$$

for (44) leads to a discrete scheme

$$\frac{\check{p}_{k+1/2} - \check{p}_k + \check{p}_k - \check{p}_{k-1/2}}{h} - \frac{\check{F}_{k-1/2} + \check{F}_{k+1/2}}{2} - \check{A}(q_k)^T \frac{\lambda_{k-1/2} + \lambda_{k+1/2}}{2} = \mathbf{0} \quad (46)$$

where the midpoint approximations are

$$\begin{aligned} q_{k+1/2} &\approx \frac{1}{2}(q_k + q_{k+1}), \quad \dot{q}_{k+1/2} \approx \frac{1}{h}(q_{k+1} - q_k), \\ \check{p}_{k+1/2} &\approx \frac{1}{h}\check{M}(q_{k+1} - q_k), \quad \text{and} \quad \check{F}_{k+1/2} \approx \check{F}(q_{k+1/2}, \dot{q}_{k+1/2}, t_{k+1/2}) \end{aligned} \quad (47)$$

Note that (46) is actually a two-timestep scheme, but can be used to derived a one-timestep scheme as follows. As illustrated in Fig. 6, the scheme (46)

at endpoint k have terms in both segments $\#k$ and $\#(k+1)$. Taking the limit $t_{k-1} \rightarrow t_k$, we have

$$\lim_{h \rightarrow 0} \frac{\check{p}_k - \check{p}_{k-1/2}}{h/2} = \dot{p}_k, \quad \lim_{h \rightarrow 0} \check{F}_{k-1/2} = \check{F}_k, \quad \text{and} \quad \lim_{h \rightarrow 0} \lambda_{k-1/2} = \lambda_k \quad (48)$$

which shows that the terms in segment $\#k$ tend to (44), so they can be dropped, leaving

$$\dot{p}_{k+1/2} - \dot{p}_k - \frac{h}{2}\check{F}_{k+1/2} - \frac{h}{2}\check{A}(q_k)^T\lambda_{k+1/2} = \mathbf{0} \quad (49)$$

Similarly, taking the limit $t_{k+1} \rightarrow t_k$ in (46) leads to

$$\dot{p}_k - \dot{p}_{k-1/2} - \frac{h}{2}\check{F}_{k-1/2} - \frac{h}{2}\check{A}(q_k)^T\lambda_{k-1/2} = \mathbf{0} \quad (50)$$

Then, applying (50) to endpoint $k+1$, and combining it with (49) as well as the constraint equations, lead to a new scheme:

$$\begin{cases} \frac{1}{h}\check{M}(q_{k+1} - q_k) - \dot{p}_k - \frac{h}{2}\check{F}_{k+1/2} - \frac{h}{2}\check{A}(q_k)^T\lambda_{k+1/2} = \mathbf{0} \\ \dot{p}_{k+1} - \frac{1}{h}\check{M}(q_{k+1} - q_k) - \frac{h}{2}\check{F}_{k+1/2} - \frac{h}{2}\check{A}(q_{k+1})^T\lambda_{k+1/2} = \mathbf{0} \\ \check{\Phi}(q_{k+1}) = \mathbf{0} \end{cases} \quad (51a)$$

$$\begin{cases} \dot{p}_{k+1} - \frac{1}{h}\check{M}(q_{k+1} - q_k) - \frac{h}{2}\check{F}_{k+1/2} - \frac{h}{2}\check{A}(q_{k+1})^T\lambda_{k+1/2} = \mathbf{0} \\ \check{\Phi}(q_{k+1}) = \mathbf{0} \end{cases} \quad (51b)$$

$$\begin{cases} \dot{p}_{k+1} - \frac{1}{h}\check{M}(q_{k+1} - q_k) - \frac{h}{2}\check{F}_{k+1/2} - \frac{h}{2}\check{A}(q_{k+1})^T\lambda_{k+1/2} = \mathbf{0} \\ \check{\Phi}(q_{k+1}) = \mathbf{0} \end{cases} \quad (51c)$$

In this new scheme, (51a) and (51c) are rearranged as residual expressions

$$\mathbf{Res}(x_{k+1}) = \begin{pmatrix} -h\dot{p}_k + \check{M}(q_{k+1} - q_k) - \frac{h^2}{2}\check{F}_{k+1/2} - \frac{s_1 h^2}{2}\check{A}^T(q_k)\lambda_{k+1/2} \\ s_2\check{\Phi}(q_{k+1}) \end{pmatrix} \quad (52)$$

where $x_{k+1} = [\dot{q}_{k+1}, \lambda_{k+1/2}^T]^T$, and $s_1 = 2h^{-2}$ and $s_2 = h^{-1}$ are two scaling factors [36] that are needed for better conditioning of the Jacobian matrix

$$\mathbf{Jac}(x_{k+1}) = \frac{\partial \mathbf{Res}}{\partial x_{k+1}} = \begin{bmatrix} \check{M} - \frac{h^2}{2}\frac{\partial\check{F}_{k+1/2}}{\partial\dot{q}_{k+1}} & -\check{A}^T(q_k) \\ \check{A}(q_{k+1}) & \mathbf{0} \end{bmatrix} \quad (53)$$

The residual (52) and its Jacobian (53) allows us to solve for q_{k+1} and $\lambda_{k+1/2}$ using the Newton-Raphson iteration method. After that, they are substituted into (51b) to compute \dot{p}_{k+1} explicitly.

The complete integration procedure is summarized in Alg. 1.

Algorithm 1: Modified symplectic integration scheme

input : initial values q_0 and \dot{q}_0 ; timestep h , total steps N ;
maximum iteration s_{max} , tolerance ϵ_{tol}

```

p0 ← Mq̇0;
for k ← 0 to N - 1 do
    q̇k+1 ← q̇k;
    λk+1/2 ← 0;
    xk+1 ← [q̇k+1, λk+1/2]^T;
    for s ← 1 to smax do /* Newton-Raphson iteration */
        compute Res by (52);
        if ||Res|| > εtol then
            compute Jac by (53);
            Δx ← -(Jac)-1Res;
            xk+1 ← xk+1 + Δx;
        else
            break;
        end
    end
    end
    compute ṗk by (51b);
    q̇k ← M-1(ṗk - Mq̇k);
end

```

6. Numerical examples

Numerical studies of several dynamic examples are presented in this section. Its aim is three-fold: (1) To verify the proposed modeling framework of tensegrity systems and the nonlinear dynamic integration scheme, by comparing against reference results, including trajectories, natural frequencies, and mode shapes; (2) To show the proposed approach's ability to perform nonlinear dynamic analyses with complex conditions, including conservative and non-conservative tension forces, cable-based actuators, gravity loads, and moving boundaries. (3) To show the proposed approach's ability to study the dynamics of tensegrity systems that include both arbitrary rigid bodies and rigid bars. In particular, we present a 2D Class-3 tensegrity tower and a 3D Class-2 deployable tensegrity structure, which exemplify new ways to compose tensegrity structures.

6.1. Example 1: Dynamics of a double pendulum

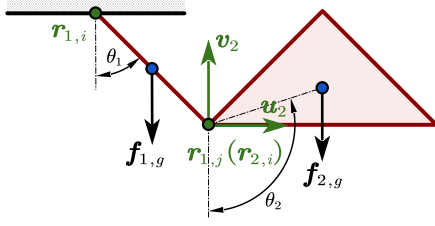


Figure 7: Schematic diagram of a double pendulum in the presence of gravity.

Table 1: Physical parameters of rigid members in example 1.

| | Parameter | Value |
|--------------------------|-------------------|---------------------------------------|
| Bar | Mass | 0.026 93 kg |
| | Moment of Inertia | $1.122 \times 10^{-5} \text{ kg m}^2$ |
| | Length | 0.070 71 m |
| Isosceles right triangle | Mass | 0.1271 kg |
| | Moment of Inertia | $7.063 \times 10^{-5} \text{ kg m}^2$ |
| | Height | 0.050 00 m |

This example is a planar double pendulum, composed of a rigid bar and an isosceles right triangular rigid plate, and subjected only to gravity forces. The initial configuration is shown in Fig. 7. It is different from the conventional two-bar double pendulum, and, as such, serves to test some fundamental ingredients of the proposed natural coordinates framework for tensegrity system dynamics. Specifically, the rigid bar's endpoints are chosen as two basic points $r_{1,i}$ and $r_{1,j}$, while the latter is shared as a vertex ($r_{2,i}$) of the triangle, which additionally requires two base vectors u_2 and v_2 to form the RUV type natural coordinates (Refer to Sec. 2.1.2). Besides, the pivot point $r_{1,i}$ is prescribed with constant coordinates (Refer to Sec. 3.2). Physical parameters of the two rigid members are listed in Tab. 1.

More importantly, this example is chosen to check if the proposed non-minimal formulation with the integration scheme Alg. 1 can produce accurate results for nonlinear rigid body dynamics, both in short-time and long-time simulations. In particular, it should be comparable with the minimal formulation, which uses the two angles θ_1 and θ_2 as generalized coordinates and leads to a set of ordinary differential equations (ODEs), and then simulated by a 5th order Runge-Kutta method with a maximum timestep $h_{\max} = 1 \times 10^{-5}$ s. Fig. 8 plots the time histories of the angles and angular velocities for 4-second simulations of dynamics. It shows the proposed approach, even when using a much larger timestep $h = 1 \times 10^{-3}$ s, produces results that are in good agreement with the reference solutions, and accurately captures the nonlinear dynamic behaviors of the double pendulum, especially the abrupt changes of angular velocities.

For long-time simulations, the proposed DAE integration scheme is compared against the generalized- α scheme which uses a typical spectral radius $\rho_\infty = 0.7$. Note that the double pendulum system is conservative, meaning that there are no non-conservative forces such as friction and damping, and that the mechanical energy $E = T + V$ should be conserved. As shown in Fig. 9, for 500-second simulations the system's energy E is mostly conserved by the proposed method, but gradually damped out by the generalized- α scheme. This is reasonable because the spectral radius ρ_∞ controls the numerical damping, which is important to ensure a stable solution for the generalized- α scheme. On the other hand, the proposed modified symplectic scheme has no numerical damping for conservative systems. Therefore, it is expected to be more suitable for long-time simulations of systems with low physical damping, such as tensegrity systems.

6.2. Example 2: A 2D Class-3 tensegrity tower

This example is a new design of 2D tensegrity structure: 4 rigid bars, 3 isosceles right triangular rigid plates, and 12 cables compose a 3-level tower, as shown in Fig. 10. The vertices of triangles are pin jointed with up to two bars: the apex of triangle ⑤ connect both bars ④ and ⑥, while other vertices connect at most one bar. Thus, it is a Class-3 tensegrity structure by definition.

Due to the presence of pin joints, the structure's DoFs are reduced to 5. It is pre-stressed redundantly by 12 cables, which have the same stiffness coefficient

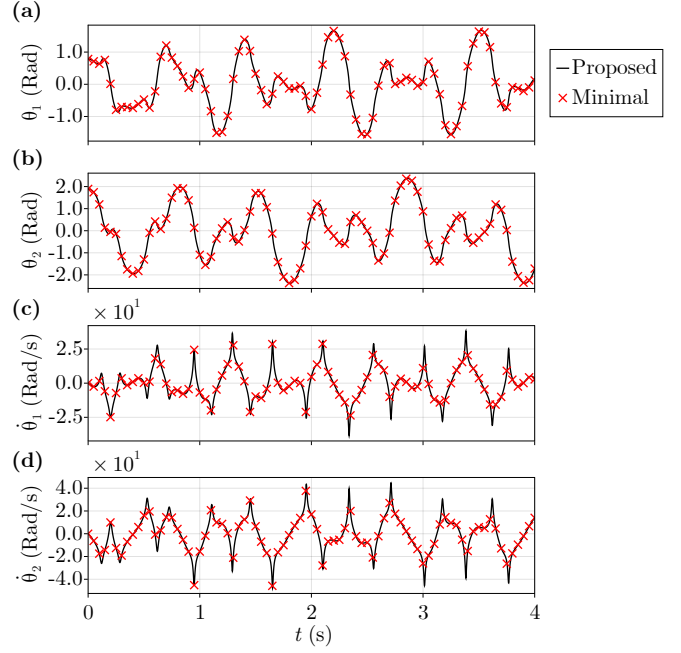


Figure 8: Time histories of angles (a) θ_1 , (b) θ_2 and angular velocities $\dot{\theta}_1$ and $\dot{\theta}_2$ of the double pendulum.

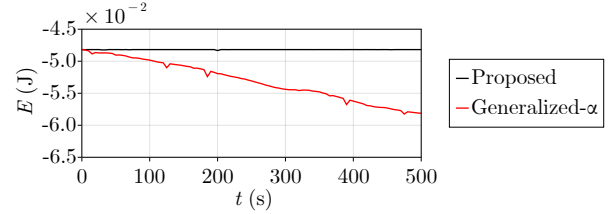


Figure 9: Time history of the mechanical energy E of the double pendulum.

κ and damping coefficient η . Additionally, the cables 3 to 12, which are essential to the integrity of structure, have rest lengths being α times their initial length. Cables 1 and 2, which provides auxiliary tensions, have rest lengths being β times their initial lengths. Tab. 2 lists the physical parameters of rigid members and cables for this example. Such a bilateral symmetric setup of geometry and distribution of tension forces ensures an initial static equilibrium of the structure.

Table 2: Physical parameters of rigid members and cables in example 2.

| | Parameter | Value |
|---------------------------|--------------------------------|---|
| Bars | Mass | 0.026 93 kg |
| | Moment of Inertia | $2.245 \times 10^{-5} \text{ kg m}^2$ |
| | Length | 0.1000 m |
| Isosceles right triangles | Same as Example 1 | |
| | Stiffness coefficient κ | 100 N m^{-1} |
| Cables | Damping coefficient η | 0 N s m^{-1} or $0.1000 \text{ N s m}^{-1}$ |
| | Rest length | $\alpha \times \text{Initial length}$ for $j = 1, 2$ $\beta \times \text{Initial length}$ for $j = 3, \dots, 12$ |

Figure 10 also illustrates how to model this structure by arranging the basic points and base vectors to form natural coordinates: three triangles ③, ⑤, and ⑦ use the three types of natural coordinates RUV, RRV, and RRR, respectively; pin joints are modeled either by the sharing of basic points, such as $r_{1,j}$ and $r_{3,i}$, or by extrinsic constraints, such as that at $r_{2,j}$; the basic points on the ground $r_{1,i}$, $r_{2,i}$, $r_{0,1}$, and $r_{0,2}$ make up the prescribed coordinates.

Therefore, this example covers all the ingredients that are needed to comprehensively test the proposed approach for the dynamics of general 2D tensegrity systems. In the rest of this section, the proposed approach is used to conduct

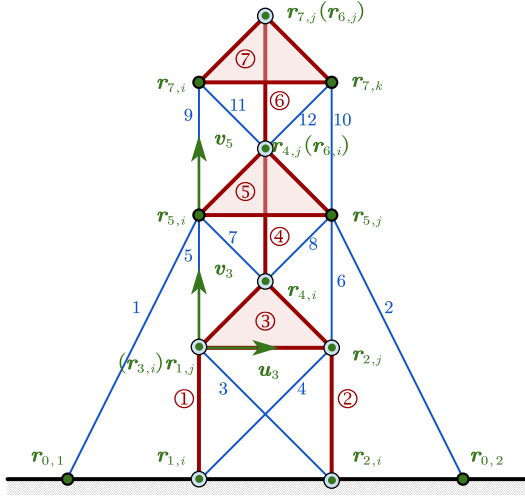


Figure 10: Schematic drawing of the 2D Class-3 tensegrity tower.

modal analyses and nonlinear dynamic analyses to investigate the effects of cables' properties on the structure's dynamics. The results are also compared with the commercial software Adams for verification.

6.2.1. Modal analysis

Since the structure is initially in static equilibrium, its dynamics can be linearized, following the procedure in Sec. 5.2.

Referring to the structure's 3-stage kinematics, it is easy to identify that the first (lowest) stage, consisting of one triangle two bars, has 1 DoF. The second (or third) stage, consisting of one triangle and one bar, has 2 DoFs. However, due to the interconnection through tensile cables, the three stages are highly coupled in dynamics. For a linear (or linearized) system, modal analysis resolves this coupling by decomposition into independent vibration modes, described in terms of natural frequencies and mode shapes. Therefore, accurate calculations of these modal data are important to understand the inherent characteristics of structural dynamics.

For stiffness coefficient $\kappa = 100 \text{ N m}^{-1}$ and rest length ratios $\alpha = \beta = 0.9$, Figs. 11 to 13 show that the natural frequencies and mode shapes produced by the proposed approach are in good agreement with Adams. The maximum relative error of natural frequencies is 4×10^{-9} . And the mode shapes are also reliably computed by the transformation from independent variables to natural coordinates.

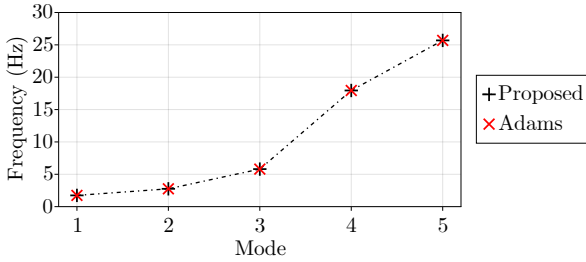


Figure 11: Natural frequencies of the 2D tensegrity tower with respect to the order of vibration mode by the proposed approach and Adams.

The noticeably low fundamental frequency (1.7371 Hz) indicates the softness of the structure. Shortening cables' rest lengths can increase the pre-stress level of tensegrity structures, and is shown to be one of the effective ways to change, but not always increase, the natural frequencies. For example, when the pre-stress level increases through reducing rest lengths, [37] shows natural frequencies of tensegrity structures generally increase, but [38] shows that the lowest natural frequency decreases due to buckling of bars. Here, we also investigate the effects of pre-stress level on the structure's stiffness. Setting the rest length ratios α and β from 0.845 to 0.999, the computed natural frequencies are shown in Fig. 14. An interesting phenomenon is observed: when the pre-stress level increases through shortening the cables, the highest two natural frequencies increase, but the lowest three ones decrease. In particular, the lowest natural frequency reaches zero at $\alpha = \beta = 0.845$, meaning a loss of structural

stability. This result is verified by Adams, which are shown as marker points in Fig. 14. This phenomenon bears notable relationship to the planar Class-2 tensegrity mechanism in [39], where the researchers also found the structural stability is lost when reducing cables' rest lengths. However, further analysis of this instability behavior is beyond the scope of this paper.

6.2.2. Numerical analysis of nonlinear dynamics

The next question is whether the structure can sustain complex excitation and loading forces, thus requiring numerical analysis of nonlinear dynamics.

The above results show that, to ensure stability of the initial configuration, the cables must not be shortened too much. However, the cables must also not be loosened too much, so as to prevent slacking, which leads to the loss of tension and can eventually result in the collapse of structure. For this reason, we set the rest length ratios $\alpha = 0.95$ and $\beta = 0.998$.

In order to be comparable with Adams, three constitutive laws of cables, derived from (28), are considered:

- (1) (UN) Undamped and no slacking: $f_j = \kappa(l_j - \mu_j)$ with $\kappa = 100 \text{ N m}^{-1}$;
- (2) (DN) Damped and no slacking: $f_j = \kappa(l_j - \mu_j) + \eta \dot{l}_j$ with $\kappa = 100 \text{ N m}^{-1}$ and $\eta = 0.1 \text{ N s m}^{-1}$;
- (3) (US) Undamped and slacking: if $l_j - \mu_j > 0$, then $f_j = \kappa(l_j - \mu_j)$, else $f_j = 0$.

Note that Adams has no built-in support for slack cables, so the US setup can only be approximated by spline interpolations.

For external excitation, we consider a sine seismic wave $x = 0.01 \sin(6\pi t)$ m on the ground as a moving boundary condition, which can be easily exerted through the prescribed coordinates in the proposed approach. To investigate the effects of the auxiliary cables, we additionally consider:

- (4) (US-AUX) Same as the US case, except that the seismic wave is exerted only on the bar's endpoints $r_{1,i}$ and $r_{2,i}$, while the cables's anchor points $r_{0,1}$ and $r_{0,2}$ remain constant.

All four setups are accompanied by gravity forces along the negative y -axis.

Nonlinear dynamic simulations are then carried out using the proposed integration scheme Alg. 1 for 2 s or until the structure collapses. The time histories of the x -coordinate of the centroid of triangle ③ is plotted in Fig. 15. It shows a good agreement with Adams, especially for the UN and DN setups. The discrepancies for the US and US-AUX setups are relatively larger, due to the spline approximation used in Adams.

Figure 16 visualizes the structures in the four setups at $t = 1.23$ s, which is the time when the structure in the US setup is collapsing: beyond this time the structure will never swing back and will eventually touch the ground. The cables with their current lengths shorter than rest lengths are drawn by blue dash lines. In the UN and DN setups these are actually springs in compression, while in the US and US-AUX setups these are the cables that go slack.

Figure 17 compares the occurrences of cables' slacking in the US and US-AUX setups. It shows that almost all cables in the US setup and only four ones in the US-AUX setups went through slacking. And at the time $t = 1.23$ s, 6 cables, including 5 essential ones, are in sustained slacking in the US setup, but only 1 auxiliary one is so in the US-AUX setup. These results suggest that the auxiliary cables can provide stabilizing support if their anchor points are fixed.

6.3. Example 3: A 3D deployable tensegrity structure

This example is a 3D multi-stage deployable tensegrity structure, which is a new design in the tensegrity literature to the best of our knowledge. It can be decomposed into three kinds of tensegrity modules:

- (1) A Class-1 tensegrity module composed of two rigid tetrahedrons and six cables, including three outer cables and three inner ones, as shown in Fig. 18(a). Since the two tetrahedrons are not jointed but instead maintain a proper separation through cables' tension forces, it is a Class-1 tensegrity module. It is also known as a 2-segment Tetraspine in the robotics literature, because it resembles the spine of vertebrate;
- (2) A Class-2 tensegrity module composed of two jointed rigid tetrahedrons and three cables, as shown in Fig. 18(b). This module bears similarity to the dual-triangle planar tensegrity mechanism [39]. But instead of being limited to planar motions, it can realize spatial rotations around the joint, either passively or actively;
- (3) A 2-stage tensegrity prism module, also known as tensegrity triplex, composed of six bars and twelve cables, as shown in Fig. 18(c). Tensegrity prism is one of the earliest kinds of "bars-only" tensegrity structures [3] with a notable feature of deployability through cable-based actuation

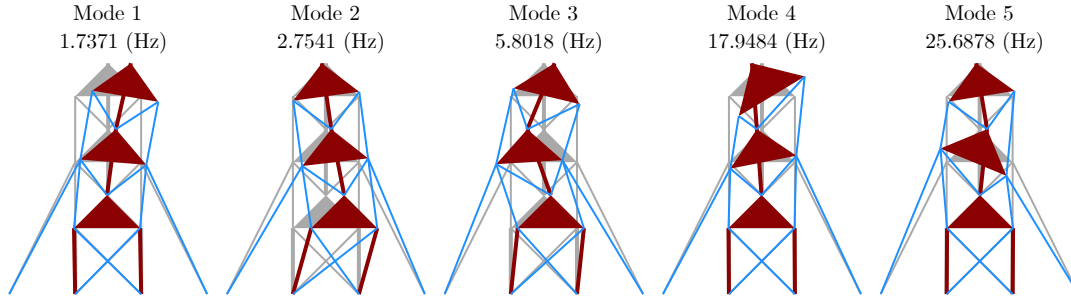


Figure 12: All five mode shapes of the 2D tensegrity tower obtained by the proposed approach.

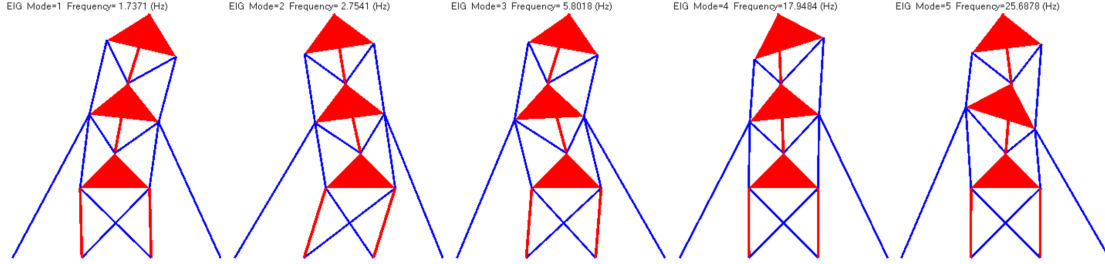


Figure 13: All five mode shapes of the 2D tensegrity tower obtained by Adams.

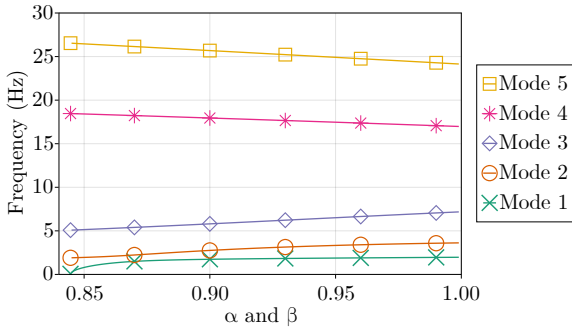


Figure 14: Natural frequencies of the 2D tensegrity tower with respect to rest length proportions α and β .

[37, 40]. For simplicity, here we assume that each cable can be actuated independently. Fig. 18(d) shows how the 2-stage prism is unfolded after deployment.

These modules compose the whole structure using the tetrahedrons as interfaces. First, the uppermost three cables of the 2-stage prism are replaced by a tetrahedron. Then, a Class-1 module, a Class-2 module, and another Class-1 module are stacked upon the prism one by one. The physical parameters of rigid members and cables for this example are listed in Tab. 3.

This new structure is one of the few examples in the literature that integrate both 3D rigid bodies and 3D rigid bars into one tensegrity system. In this way, it also integrates the functionalities of different modules: in the lower part, the 2-stage prism provides deployability; in the upper part, the Class-2 module provides the function of orientation-tuning, while the Class-1 modules can be used for vibration isolation. In this paper, we focus on its deployability feature, leaving the investigation of other applications to in-depth studies in the future. The structure's configurations before and after deployment are referred to as the initial and target configurations, as shown in Fig. 18(e) and (f), respectively.

To test the proposed modeling approach and numerical integration method, we consider the problem of deployment simulation in a dynamic environment.

Modeling of the structure is straightforward using the natural coordinates approach. Working from top to bottom, the rigid tetrahedrons can be modeled by whatever types of natural coordinates for 3D rigid bodies, but for the purpose of verification, the four types of natural coordinates RUVW, RRVW, RRRW, and RRRR are used for the four tetrahedrons ⑩, ⑨, ⑧, and ⑦, respectively; For the 2-stage prism, endpoints of the rigid bars are used as basic points, and those which are jointed to the ground become the prescribed coordinates; Lastly, all ball joints are automatically modeled by the sharing of basic points.

Table 3: Physical parameters of rigid members and cables in example 3.

| | | Parameter | Value |
|--------------|---------------------------------------|-----------|--|
| Bars | Mass | | 0.080 00 kg |
| | Moment of Inertia | | 0.000 322 7 kg m ² |
| | Length | | 0.2200 m |
| Tetrahedrons | Mass | | 0.2999 kg |
| | Center of mass | | at height 0.014 82 m |
| | Principal moments of Inertia | | 7.664 × 10 ⁻⁴ kg m ² , 7.664 × 10 ⁻⁴ kg m ² , 1.246 × 10 ⁻³ kg m ² |
| | Circumradius of base regular triangle | | 0.010 00 m |
| Cables | Height | | 0.070 71 m |
| | Stiffness coefficient | | 1000 N m ⁻¹ for the 2-stage prism 500 N m ⁻¹ for others |
| | Damping coefficient | | 2 N s m ⁻¹ |
| | Rest length | | See text and Tab. 4 |

Degrees of freedom can be worked out algebraically as follows. Originally, four rigid tetrahedrons have $4 \times 6 = 24$ DoFs, while six bars have $6 \times 5 = 30$ DoFs. Ten ball joints, including one between ⑨ and ⑧, six for the ends of bars ④ to ⑥, and three between bars ① to ③ and the ground, impose $10 \times 3 = 30$ constraints. Therefore, the system has $24 + 30 - 30 = 24$ DoFs.

To implement the cable-based actuation for deployment simulations, the rest lengths of the first nine cables $\mu_1(t)$ to $\mu_9(t)$ are specified as functions of time t . On the other hand, the dynamic environment is exemplified by a sine seismic wave $x(t) = 0.01 \sin(\nu 2\pi t)$ with a seismic frequency ν of the ground, which is implemented by use of the prescribed coordinates.

Many studies on deployable tensegrity structures generally regard the deployment as a quasi-static process [9, 41] or a sequence of static equilibria [5], and assume that the dynamic effects can be neglected if the deployment time is sufficiently large. This assumption is obviously not warranted for deployments in dynamic environments, where various factors, such as a moving base, wind loadings, or impact events, could have long-term or short-term effects and hinder the success of deployments.

However, this quasi-static view can predict certain dynamic behaviors during deployment. Consider the seismic frequency ν that sits between the natural frequencies of an initial state and a target state. If the structure's static equilibrium varies continuously, the structure's natural frequencies would also vary continuously from the initial state to the target state. Therefore, there must be

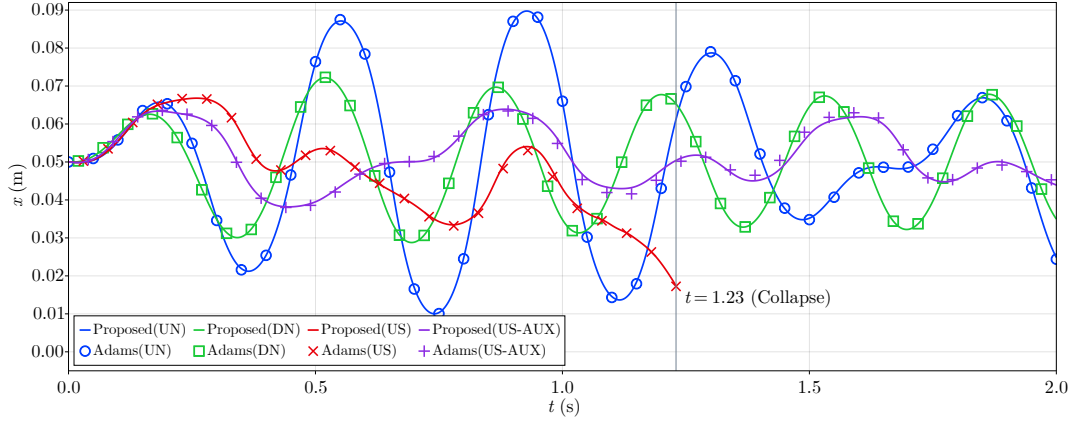


Figure 15: Time histories of the x -coordinate of the centroid of triangle ③ for the UN, DN, US, and US-AUX setups.

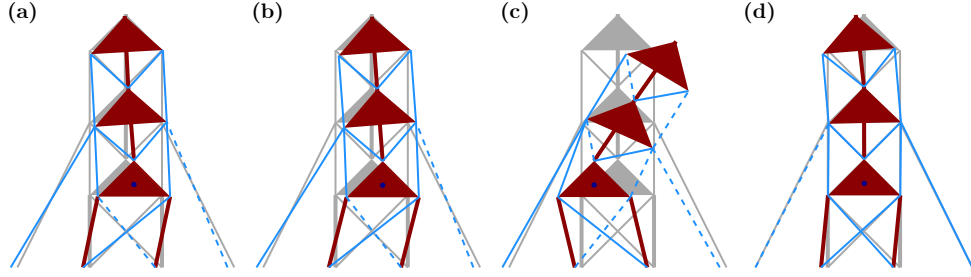


Figure 16: Snapshots of the 2D tensegrity tower at time $t = 1.23$ s for the (a) UN, (b) DN, (c) US, and (d) US-AUX setups. Blue dashed lines represent (a,b) compressed or (c,d) slack cables.

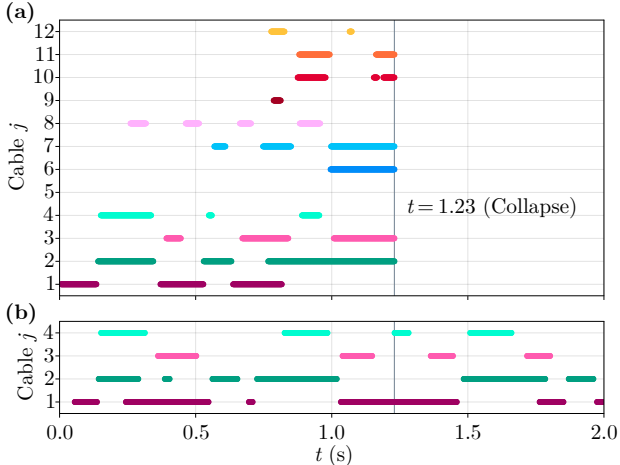


Figure 17: Occurrences of cables' slacking in the US and US-AUX setups.

an intermediate state which resonates with this specific seismic frequency, and consequently leads to severe vibrations or even collapse.

In what follows, we will verify this prediction and thereby testing our proposed approach for the dynamic analysis of tensegrity structures. First, the statics and dynamics of the structure in the initial and target states are examined in Secs. 6.3.1 and 6.3.2. Then, deployment simulations are conducted in Sec. 6.3.3.

6.3.1. Inverse statics and modal analysis

Both initial and target configurations are straightly upright, as shown in Fig. 18(e) and (f). Therefore, they are uniquely defined by the distances between tetrahedrons d , the height of a prism stage h , and the circumradiuses r_1 and r_2 , which are listed in Tab. 4.

Since the system has 24 DoFs and 24 cables, the matrix \mathbf{B} in (32) is of dimension 24×24 . But for both initial and target configurations, the rank of matrix \mathbf{B} is 21, which means the equations (32) have a 3-dimensional solution set. This is because the Class-1 and Class-2 modules have non-unique solutions for the rest lengths. The Class-2 module can achieve static equilibrium as long

as all three cables have the same rest lengths. In the Class-1 module, tension forces of outer cables are determined from the vertical loading as well as the inner cables. Therefore, in order to have a unique solution for the rest lengths, we first specify $\mu_{16} = \mu_{17} = \mu_{18} = 0.1$ m and $\mu_{13} = \mu_{14} = \mu_{15} = \mu_{19} = \mu_{20} = \mu_{21} = 0.03$ m. Then, substituting these values into (32) allows to solve for other rest lengths. The results are listed in Tab. 4, which together with Tab. 3 completely defines the initial and target static states. As expected, only the first nine cables' rest lengths need to be varied for the deployment. We also verify that there is no slack cable in either state.

Modal analyses are then conducted for both initial and target states to compute the natural frequencies. Note that, different from example 2, gravity is taken into account here for the static equilibrium and consequently in the model analyses. Therefore, the computed natural frequencies can reveal the dynamic properties of the structure subject to gravity, which is closer to the real world situations. Fig. 19 shows the first five natural frequencies, excluding duplicates, for both states. Of particular interest is the decrease of the lowest natural frequency from 0.7184 Hz to 0.3270 Hz. This can be attributed to the combined effects of the structure's elevated mass center, the decrease of circumradius r_2 , and the loosening of some cables.

6.3.2. Seismic simulations

Next, we conduct seismic simulations for both initial and target configurations, starting from their static equilibrium states. The seismic frequency is set to $\nu = 0.5$ Hz, which sits approximately in the middle of the two states' lowest natural frequencies.

Fig. 20 plots the trajectories in the x and z coordinates of mass centers of the tetrahedrons ⑦ to ⑩ for 15-second seismic simulations. The y coordinates' changes are smaller than the x coordinates by one order of magnitude, thus not shown. None of the magnitudes of responses in any coordinates increase with time. These results show that, as expected, the structure starting from both initial and target states undergoes forced vibrations but no resonance with the seismic wave.

6.3.3. Deployment simulations

In order to conduct deployment simulations, the actuation strategy of the cables' rest lengths must be specified. Specifically, the rest length of the j th

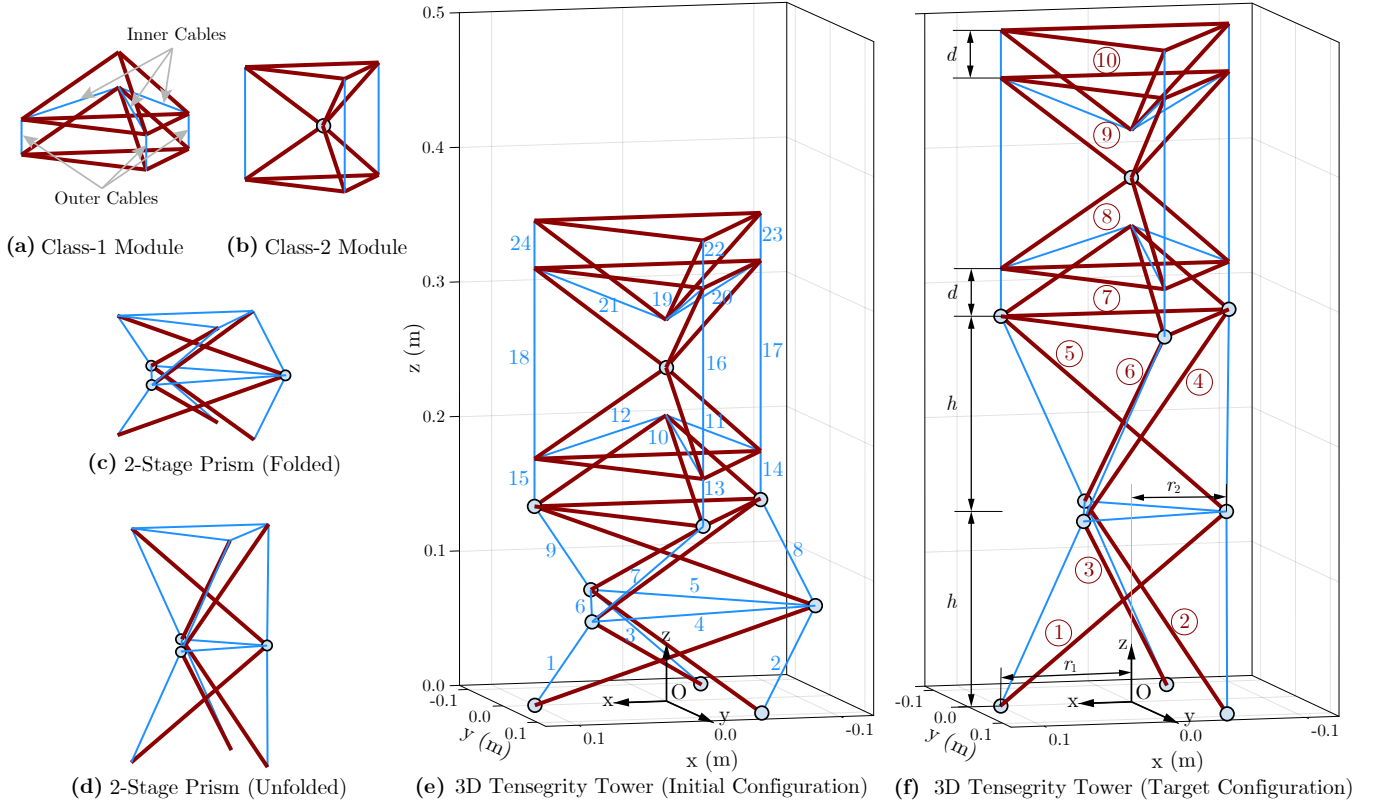


Figure 18: Schematic drawings of (a) a Class-1 tensegrity module, (b) a Class-2 tensegrity module, (c) a folded and (d) an unfolded 2-stage prism, and the (e) initial and (f) target configurations of the 3D deployable tensegrity structure.

Table 4: Physical parameters of initial and target configurations in example 3.

| | Label | Initial | Target |
|----------------------|--------------|------------|------------|
| Distance | d | 0.035 36 m | 0.035 36 m |
| Height | h | 0.070 71 m | 0.1414 m |
| Circumradius | r_1 | 0.1000 m | 0.1000 m |
| | r_2 | 0.1100 m | 0.070 00 m |
| Cables' rest lengths | (1, 2, 3) | 0.1039 m | 0.1545 m |
| | (4, 5, 6) | 0.1677 m | 0.1109 m |
| | (7, 8, 9) | 0.1045 m | 0.1550 m |
| | (10, 11, 12) | 0.072 35 m | 0.072 35 m |
| | (13, 14, 15) | 0.030 00 m | 0.030 00 m |
| | (16, 17, 18) | 0.1000 m | 0.1000 m |
| | (19, 20, 21) | 0.030 00 m | 0.030 00 m |
| | (22, 23, 24) | 0.084 12 m | 0.084 12 m |

cable is implemented as a function of time

$$\mu_j(t) = (1 - \tau(t))\mu_{j,0} + \tau(t)\mu_{j,1}$$

where the coefficient τ takes values from 0 to 1; the initial and target values $\mu_{j,0}$ and $\mu_{j,1}$ are taken from Tab. 4. For simplicity, a linear actuation strategy is used: before the deployment duration T_d , the coefficient τ varies linearly, after that, τ remains unchanged, as shown in Fig. 21.

Deployment simulations are then carried out on seismic grounds with different deployment durations $T_d = 5$ s, 10 s, 15 s and 20 s and different seismic frequencies $\nu = 0.2$ Hz, 0.5 Hz and 1.0 Hz. Note that the frequencies $\nu = 0.2$ Hz and 1.0 Hz are outside of the expected resonance range [0.7184, 0.3270] Hz and also avoid other natural frequency ranges. Deployment simulations on static ground are also conducted to provide reference solutions.

For $T_d = 10$ s and $\nu = 0.5$ Hz, snapshots of the structure at times $t = 1$ s, 5.5 s and 10 s are visualized in Fig. 22. For all deployment simulation cases, trajectories in the x and z coordinates of the mass center of tetrahedron ⑩ are plotted in Fig. 23.

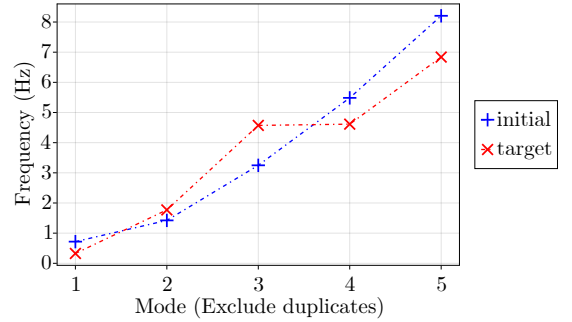


Figure 19: First five natural frequencies, excluding duplicates, of the 3D tensegrity structure in the initial and target states.

These results show that, for $T_d = 10$ s, 15 s and 20 s, the structure's dynamic behaviors with the frequency $\nu = 0.5$ Hz are similar and can be divided into three courses:

- (1) In the beginning of deployments, the magnitudes of responses of the structure remain steady, which is exemplified by Fig. 22(a).
- (2) In the middle of deployments, the magnitudes of responses increase, shows the signs of resonance, which is exemplified by Fig. 22(b).
- (3) Near the end of deployments, the structure inclines towards the positive x direction before collapsing. Additionally, one or more cables can go slack at this time. This is exemplified by Fig. 22(c), where the first cable is slack.

For $T_d = 5$ s, the behavior is a bit different: the structure collapses later at 16 seconds after, instead of during, the deployment. This can be explained by the shorter duration of resonance, which nonetheless has long-term effects on the structure.

Therefore, these results agree well with the prediction about resonance, and thereby demonstrate the proposed approach's abilities to model general tensegrity structure and perform difficult dynamic analyses involving deployments, dynamic environments, and slack cables.

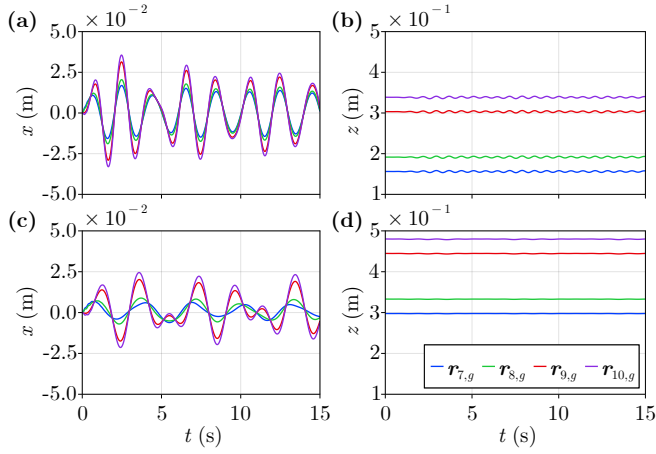


Figure 20: Time histories of the (a,c) x and (b,d) z coordinates of $r_{7,g}$, $r_{8,g}$, $r_{9,g}$, and $r_{10,g}$ for the 3D tensegrity structure starting from the (a,b) initial and (c,d) target states.

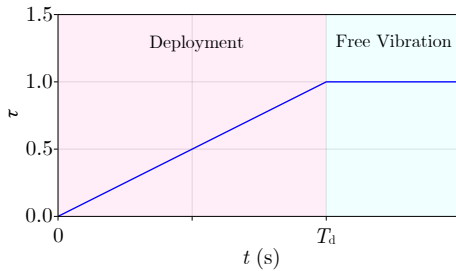


Figure 21: Actuation coefficient $\tau(t)$ as a function of time t .

7. Conclusion

In this paper, a unified framework based exclusively on non-minimal coordinates (i.e. natural coordinates) are developed for dynamic analysis tensegrity structures with arbitrary rigid bodies and rigid bars. By doing so, the singularity and ill-definedness problems in minimal formulations of rigid bars are avoided, and the advantages of non-minimal formulations are retained in the system's dynamics. Namely, the resulting dynamic equation has a constant mass matrix, and is free from trigonometric functions as well as centrifugal and Coriolis terms.

The natural coordinates are comprehensively reformed. Four, three, and two types of natural coordinates are derived for a 3D rigid body, a 2D rigid body, and a 3D or 2D rigid bar. Different types of natural coordinates represent different arrangements of basic points and base vectors, and hence give much flexibility to model joints between rigid bodies or between rigid bodies and rigid bars. These different types of coordinates are then abstracted and unified into a universal transformation relation (13). By employing the idea of polymorphism, not only mathematical symbols are simplified in the derivations of dynamics but also generic computer codes are made possible.

Solution methods are also developed to enable complete analyses of tensegrity structures under the same framework. Static analysis methods are formulated to determine the static equilibrium states of tensegrity configurations. By taking into account the separation of free and prescribed coordinates in the Lagrange-d'Alembert principle, a set of DAEs is derived for the nonlinear dynamics of tensegrity systems. Numerical analysis of nonlinear dynamics is enabled by deriving a symplectic integration scheme with modifications adapted to non-conservative forces. Modal analysis is also enabled by the linearizing the governing DAEs around static equilibrium and using the reduced-basis method, so that the inherent dynamic characteristics, such as natural frequencies and mode shapes, can be easily calculated.

The proposed modeling framework of tensegrity systems and the modified symplectic integration scheme are comprehensively verified by comparing against reference results when possible. In particular, numerical integration solutions are very close to those from minimal formulations, even when a much larger timestep is used. And the relative error of natural frequencies between the proposed approach and the commercial software Adams is 4×10^{-9} .

Situations where it is hard to make direct comparisons with reference results are also investigated. Different constitute laws are considered in the seismic

simulations of the 2D tensegrity tower, shows the proposed approach's ability to deal with non-conservative tension forces, including multiple slacking events in the cables. The nonlinear dynamics of a 3D deployable tensegrity structure with 6-DoF rigid bodies and 5-DoF rigid bars is simulated, which is hard if not impossible in most commercial softwares. Simulations of cable-based deployments on a seismic ground under gravity loads also demonstrate the ability to cope with complex and real-world conditions.

cable-based deployments on a seismic ground under gravity loads also demonstrate the ability to cope with complex and real-world conditions. multiple slacking events in the cables.

Furthermore, the two novel designs of tensegrity structures exemplify new ways to integrate Class-1-to- k tensegrity modules with arbitrary rigid bodies and rigid bars to create multi-functional composite structures.

References

- [1] F. R. Buckminster, Tensegrity structures (Nov. 1962).
- [2] H. Lalvani, Origins Of Tensegrity: Views Of Emmerich, Fuller And Snelson, *International Journal of Space Structures* 11 (1-2) (1996) 27–27.
- [3] R. E. Skelton, M. C. de Oliveira, *Tensegrity Systems*, Springer, Dordrecht ; New York, 2009.
- [4] H. Furuya, Concept of Deployable Tensegrity Structures in Space Application, *International Journal of Space Structures* 7 (2) (1992) 143–151.
- [5] C. Sultan, R. Skelton, Deployment of tensegrity structures, *International Journal of Solids and Structures* 40 (18) (2003) 4637–4657.
- [6] S. Krishnan, B. Li, Design of Lightweight Deployable Antennas Using the Tensegrity Principle, in: *Earth and Space 2018*, American Society of Civil Engineers, Cleveland, Ohio, 2018, pp. 888–899.
- [7] C. Sultan, Chapter 2 Tensegrity: 60 Years of Art, Science, and Engineering, in: *Advances in Applied Mechanics*, Vol. 43 of *Advances in Applied Mechanics*, Elsevier, 2009, pp. 69–145.
- [8] A. C. Sychterz, I. F. C. Smith, Using dynamic measurements to detect and locate ruptured cables on a tensegrity structure, *Engineering Structures* 173 (2018) 631–642.
- [9] N. Veuve, S. D. Safaei, I. F. C. Smith, Deployment of a Tensegrity Footbridge, *Journal of Structural Engineering* 141 (11) (2015) 04015021.
- [10] A. G. Tibert, S. Pellegrino, Deployable Tensegrity Reflectors for Small Satellites, *Journal of Spacecraft and Rockets* 39 (5) (2002) 701–709.
- [11] C. Sultan, M. Corless, R. T. Skelton, Peak-to-peak control of an adaptive tensegrity space telescope, in: *Smart Structures and Materials 1999: Mathematics and Control in Smart Structures*, Vol. 3667, International Society for Optics and Photonics, 1999, pp. 190–201.
- [12] M. Chen, R. Goyal, M. Majji, R. E. Skelton, Design and analysis of a growable artificial gravity space habitat, *Aerospace Science and Technology* 106 (2020) 106147.
- [13] K. Snelson, The Art of Tensegrity, *International Journal of Space Structures* 27 (2-3) (2012) 71–80.
- [14] S. M. Levin, THE TENSEGRITY-TRUSS AS A MODEL FOR SPINE MECHANICS: BIOTENSEGRITY, *Journal of Mechanics in Medicine and Biology* 02 (03n04) (2002) 375–388.
- [15] S. Lessard, J. Bruce, E. Jung, M. Teodorescu, V. SunSpiral, A. Agogino, A lightweight, multi-axis compliant tensegrity joint, in: *2016 IEEE International Conference on Robotics and Automation (ICRA)*, IEEE, Stockholm, Sweden, 2016, pp. 630–635.
- [16] B. Chen, H. Jiang, Swimming Performance of a Tensegrity Robotic Fish, *Soft Robotics* 6 (4) (2019) 520–531.
- [17] S. Liu, Q. Li, P. Wang, F. Guo, Kinematic and static analysis of a novel tensegrity robot, *Mechanism and Machine Theory* 149 (2020) 103788.
- [18] Y. Wang, X. Xu, Y. Luo, Topology design of general tensegrity with rigid bodies, *International Journal of Solids and Structures* 202 (2020) 278–298.
- [19] J. Cheong, R. E. Skelton, Nonminimal Dynamics of General Class k Tensegrity Systems, *International Journal of Structural Stability and Dynamics* 15 (02) (2015) 1450042.
- [20] Z. Kan, H. Peng, B. Chen, W. Zhong, A sliding cable element of multibody dynamics with application to nonlinear dynamic deployment analysis of clustered tensegrity, *International Journal of Solids and Structures* 130–131 (2018) 61–79.
- [21] Z. Kan, N. Song, H. Peng, B. Chen, X. Song, A comprehensive framework for multibody system analysis with clustered cables: Examples of tensegrity structures, *International Journal of Solids and Structures* 210–211 (2021) 289–309.
- [22] M. Cefalo, J. M. Mirats-Tur, A comprehensive dynamic model for class-1 tensegrity systems based on quaternions, *International Journal of Solids and Structures* 48 (5) (2011) 785–802.
- [23] R. Skelton, Dynamics and Control of Tensegrity Systems, in: G. Gladwell, H. Ulbrich, W. Günthner (Eds.), *IUTAM Symposium on Vibration Control of Non-*

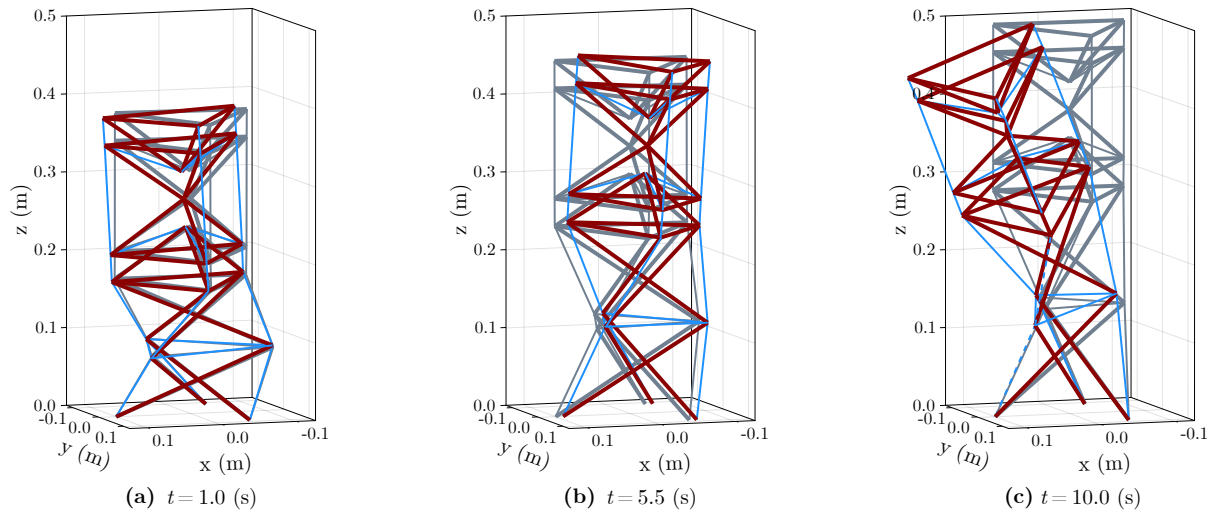


Figure 22: Snapshots at times (a) $t = 1.0$ s, (b) $t = 5.5$ s, and (c) $t = 10.0$ s of the 3D tensegrity structure deploying with a seismic frequency $\nu = 0.5$ Hz and a deployment duration $T_d = 10$ s.

linear Mechanisms and Structures, Vol. 130, Springer Netherlands, Dordrecht, 2005, pp. 309–318.

- [24] R. E. Skelton, Efficient Models of Multi-body Dynamics, in: R. Blockley, W. Shyy (Eds.), Encyclopedia of Aerospace Engineering, John Wiley & Sons, Ltd, Chichester, UK, 2010, p. eae301.
- [25] K. Nagase, R. E. Skelton, Network and vector forms of tensegrity system dynamics, Mechanics Research Communications 59 (2014) 14–25.
- [26] R. Goyal, R. E. Skelton, Tensegrity system dynamics with rigid bars and massive strings, Multibody System Dynamics 46 (3) (2019) 203–228.
- [27] S.-C. Hsu, V. Tadiparthi, R. Bhattacharya, A Lagrangian method for constrained dynamics in tensegrity systems with compressible bars, Computational Mechanics 67 (1) (2021) 139–165.
- [28] S. Ma, M. Chen, Z. Peng, X. Yuan, R. Skelton, The Equilibrium and Form-Finding of General Tensegrity Systems with Rigid Bodies, Engineering Structures (2022).
- [29] X. M. Xu, J. H. Luo, X. G. Feng, H. J. Peng, Z. G. Wu, A generalized inertia representation for rigid multibody systems in terms of natural coordinates, Mechanism and Machine Theory 157 (2021) 104174.
- [30] J. G. De Jalón, J. Unda, A. Avello, Natural coordinates for the computer analysis of multibody systems, Computer Methods in Applied Mechanics and Engineering 56 (3) (1986) 309–327.
- [31] J. Garcí'a de Jalón, J. Unda, A. Avello, J. M. Jime'nez, Dynamic Analysis of Three-Dimensional Mechanisms in "Natural" Coordinates, Journal of Mechanisms, Transmissions, and Automation in Design 109 (4) (1987) 460–465.
- [32] J. G. de Jalón, Twenty-five years of natural coordinates, Multibody System Dynamics 18 (1) (2007) 15–33.
- [33] J. Luo, Z. Wu, X. Xu, Y. Chen, Z. Liu, L. Ming, Forward Statics of Tensegrity Robots With Rigid Bodies Using Homotopy Continuation, IEEE Robotics and Automation Letters 7 (2) (2022) 5183–5190.
- [34] W. X. Zhong, Q. Gao, Integration of constrained dynamical system via analytical structural mechanics, Journal of Dynamics and Control 4 (3) (2006) 193–200.
- [35] F. Wu, W. Zhong, Constrained Hamilton variational principle for shallow water problems and Zu-class symplectic algorithm, Applied Mathematics and Mechanics 37 (1) (2016) 1–14.
- [36] O. A. Bauchau, A. Epple, C. L. Bottasso, Scaling of Constraints and Augmented Lagrangian Formulations in Multibody Dynamics Simulations, Journal of Computational and Nonlinear Dynamics 4 (021007) (Mar. 2009).
- [37] Z. Kan, H. Peng, B. Chen, W. Zhong, Nonlinear dynamic and deployment analysis of clustered tensegrity structures using a positional formulation FEM, Composite Structures 187 (2018) 241–258.
- [38] N. Ashwear, A. Eriksson, Natural frequencies describe the pre-stress in tensegrity structures, Computers & Structures 138 (2014) 162–171.
- [39] W. Zhao, A. Pashkevich, A. Klimchik, D. Chablat, Elastostatic Modeling of Multi-Link Flexible Manipulator Based on Two-Dimensional Dual-Triangle Tensegrity Mechanism, Journal of Mechanisms and Robotics 14 (2) (2022) 021002.
- [40] K. M. Roffman, G. A. Lesieutre, Cable-Actuated Articulated Cylindrical Tensegrity Booms, in: AIAA Scitech 2019 Forum, American Institute of Aeronautics and Astronautics.
- [41] N. Bel Hadj Ali, L. Rhode-Barbarigos, I. F. C. Smith, Analysis of clustered tensegrity structures using a modified dynamic relaxation algorithm, International Journal of Solids and Structures 48 (5) (2011) 637–647.

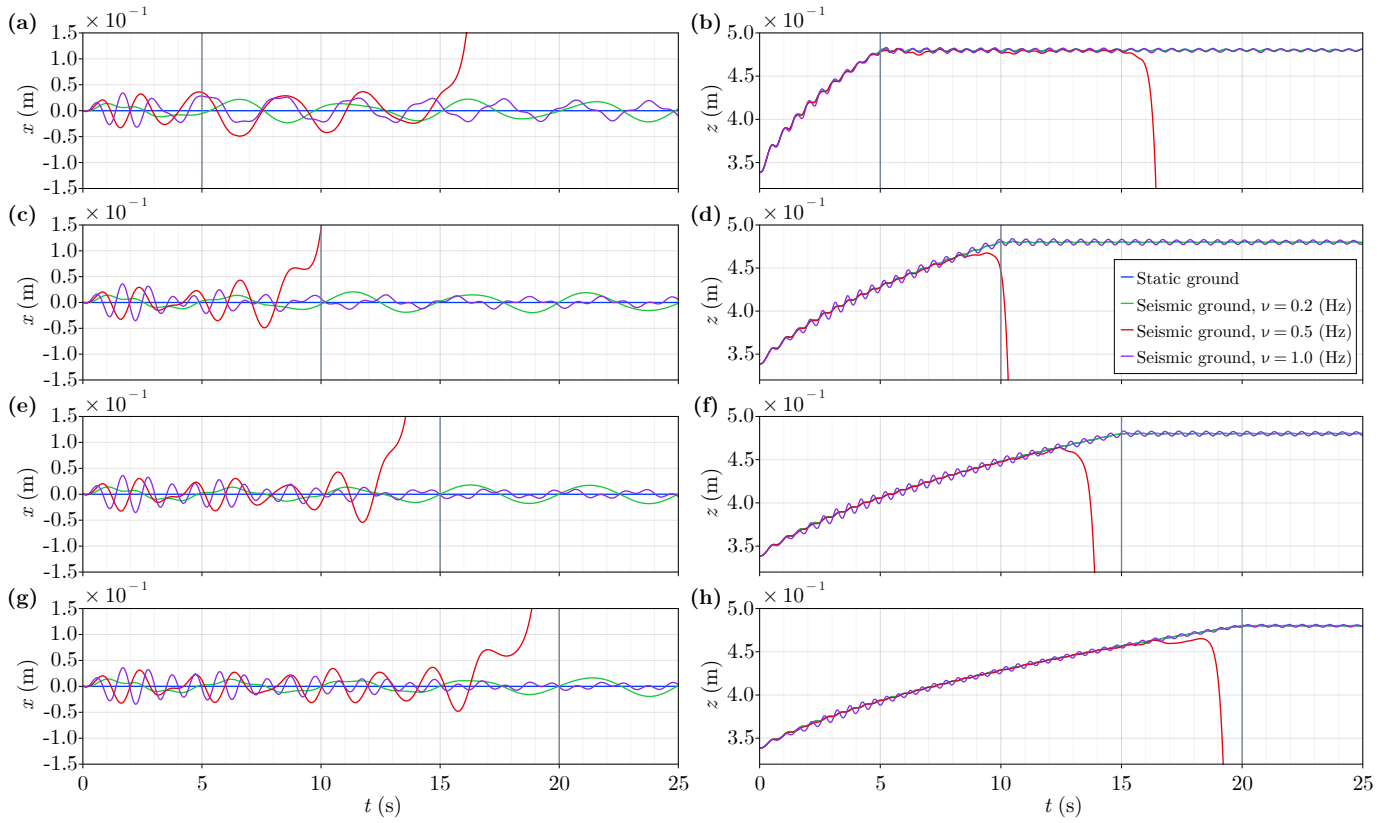


Figure 23: Time histories of the (a,c,e,g) x and (b,d,f,h) z coordinates of $\mathbf{r}_{10,g}$ for the 3D tensegrity structure with deployment durations (a,b) $T_d = 5$ s, (c,d) $T_d = 10$ s, (e,f) $T_d = 15$ s, (g,h) $T_d = 20$ s.